การประดิษฐ์โครงสร้างขนาดนาโนเมตรที่มีรูปร่างคล้ายวงแหวน จากอินเดียมแกลเลียมอาร์เซไนด์ ด้วยวิธีปลูกชั้นผลึกด้วยลำโมเลกุลแบบหยด

นางสาวนราพร ปั้นเก่า

วิทยานิพนธ์นี้เป็นส่วนหนึ่งของการศึกษาตามหลักสูตรปริญญาวิศวกรรมศาสตรดุษฎีบัณฑิต
สาขาวิชาวิศวกรรมไฟฟ้า ภาควิชาวิศวกรรมไฟฟ้า
คณะวิศวกรรมศาสตร์ จุฬาลงกรณ์มหาวิทยาลัย
ปีการศึกษา 2553

THE FABRICATION OF InGaAs RING-LIKE NANOSTRUCTURES BY DROPLET MOLECULAR BEAM EPITAXY

Miss Naraporn Pankaow

A Dissertation Submitted in Partial Fulfillment of the Requirements
for the Degree of Doctor of Philisophy Program in Electrical Engineering
Department of Electrical Engineering
Faculty of Engineering
Chulalongkorn University
Academic year 2010

Thesis Title	The Fabrication of InGaAs Ring-Like Nanostructures by Droplet Molecular Beam Epitaxy
By	Miss Naraporn Pankaow
Field of Study	Electrical Engineering
Thesis Advisor	Associate Professor Somchai Ratanathammaphan, D.Eng.
Thesis Co-advisor	Professor Somsak Panyakeow, D.Eng.
Thesis Co-advisor	Professor Charles W. Tu, Ph.D.

Accepted by the Faculty of Engineering, Chulalongkorn University in Partial Fulfillment of the Requirements for the Doctor's Degree

..... Dean of Faculty of Engineering
(Associate Professor Boonsom Lerdhirunwong, Dr.Ing.)

THESIS COMMITTEE

..... Chairman
(Professor Virulh Sa-yakanit, Ph.D.)

..... Thesis Advisor
(Associate Professor Somchai Ratanathammaphan, D.Eng.)

..... Thesis Co-advisor
(Professor Somsak Panyakeow, D.Eng.)

..... Thesis Co-advisor
(Professor Charles W. Tu, Ph.D.)

..... Examiner
(Assistant Professor Kajornyod Yoodee, Ph.D.)

..... Examiner
(Associate Professor Banyong Toprasertpong, Dr.Ing.)

..... External Examiner
(Noppadon Nuntawong, Ph.D.)

นราพร ปั้นเก่า : การประดิษฐ์โครงสร้างขนาดนาโนเมตรที่มีรูปร่างคล้ายวงแหวนจากอินเดียมแกลเลียมอาร์เซไนด์ ด้วยวิธีปลูกชั้นผลึกด้วยลำโมเลกุลแบบหยด. (THE FABRICATION OF InGaAs RING-LIKE NANOSTRUCTURES BY DROPLET MOLECULAR BEAM EPITAXY) อ. ที่ปรึกษาวิทยานิพนธ์หลัก : รศ.ดร. สมชัย รัตนธรรมพันธ์, อ. ที่ปรึกษาวิทยานิพนธ์ร่วม: ศ.ดร. สมศักดิ์ ปัญญาแก้ว, Prof.Dr. Charles W. Tu, 66 หน้า.

วิทยานิพนธ์นี้นำเสนอการประดิษฐ์โครงสร้างนาโนรูปวงแหวนของอินเดียมแกลเลียมอาร์เซไนด์ด้วยวิธีปลูกชั้นผลึกด้วยลำโมเลกุลแบบหยด โดยมีการแปรเงื่อนไขในการขึ้นรูปหยดของอินเดียมแกลเลียม เพื่อศึกษาผลของอุณหภูมิแผ่นฐานขณะขึ้นรูปหยดโลหะของอินเดียมแกลเลียม ปริมาณอินเดียมแกลเลียมที่ใช้ในการขึ้นรูปหยดโลหะ และค่าสัดส่วนอินเดียมของอินเดียมแกลเลียมที่หยดลงไป ที่มีต่อโครงสร้างนาโนรูปวงแหวนของอินเดียมแกลเลียมอาร์เซไนด์ พบว่าเมื่ออุณหภูมิแผ่นฐานขณะปลูกอินเดียมแกลเลียมสูงขึ้น จะทำให้ขนาดของโครงสร้างอินเดียมแกลเลียมอาร์เซไนด์รูปวงแหวนมีขนาดใหญ่ขึ้น แต่ค่าความหนาแน่นของจำนวนโครงสร้างนาโนลดลง เนื่องจากระยะการแพร่ของอะตอมโลหะอินเดียมและแกลเลียมมีค่าเพิ่มขึ้น ส่งผลทำให้หยดของอินเดียมแกลเลียมแผ่ขยายไปในทิศทางสองมิติและหลอมรวมตัวกับหยดที่อยู่ใกล้เคียง ในทางเดียวกันการเพิ่มปริมาณอินเดียมแกลเลียมที่ใช้ในการขึ้นรูปหยดโลหะทำให้ขนาดของโครงสร้างอินเดียมแกลเลียมอาร์เซไนด์รูปวงแหวนมีขนาดใหญ่ขึ้นในกรณีที่อุณหภูมิแผ่นฐานขณะหยดต่ำ (150 องศาเซลเซียส) แต่ความหนาแน่นของโครงสร้างรูปวงแหวนแปรเปลี่ยนไปมาเมื่อเพิ่มปริมาณอินเดียมแกลเลียม อันเป็นผลมาจากการรวมตัวของหยดอินเดียมแกลเลียมขนาดเล็กจนกลายเป็นชั้นเรียบแทนที่จะเป็นหยดเดี่ยวๆ สำหรับกรณีที่อุณหภูมแผ่นฐานขณะหยดสูงขึ้น (210 องศาเซลเซียส) โครงสร้างนาโนรูปวงแหวนมีขนาดสูงขึ้นมีความหนาแน่นมากขึ้นแต่กลับมีขนาดเส้นผ่านศูนย์กลางลดลง อันเป็นผลมาจากความเครียด (compressive strain) ซึ่งสะสมภายในโครงสร้างนาโนรูปวงแหวนที่ใหญ่ขึ้นและเกิดการผ่อนคลายบางส่วน นอกจากนี้การแปรค่าสัดส่วนอินเดียมของอินเดียมแกลเลียมที่ใช้ในการขึ้นรูปหยดโลหะ ไปทำให้ความหนาแน่นและขนาดของโครงสร้างนาโนรูปวงแหวนเปลี่ยนไปอย่างชัดเจน ได้แก่ โครงสร้างรูปวงแหวนขนาดจิ๋วที่มีความหนาแน่นสูงเกิดจากหยดอินเดียมแกลเลียมที่มีปริมาณแกลเลียมมากกว่าอินเดียม ในขณะที่โครงสร้างรูปวงแหวนขนาดปกติที่มีความหนาแน่นต่ำเกิดจากหยดอินเดียมแกลเลียมที่มีปริมาณอินเดียมมากกว่าแกลเลียม

สำหรับการวัดคุณสมบัติทางแสง โครงสร้างนาโนรูปวงแหวนของอินเดียมแกลเลียมอาร์เซไนด์ถูกปลูกขึ้นอีกครั้งภายใต้เงื่อนไขที่เลือกและปลูกกลบด้วยชั้นของแกลเลียมอาร์เซไนด์หนา 100 นาโนเมตร ประกอบด้วยชั้นแกลเลียมอาร์เซไนด์ที่ปลูกด้วยโดยวิธีไมเกรชัน-เอนฮานซ์อิพิแทกซี (migration-enhanced epitaxy) และชั้นแกลเลียมอาร์เซไนด์ที่ปลูกด้วยวิธีปกติ คุณสมบัติทางแสงของโครงสร้างรูปวงแหวนของอินเดียมแกลเลียมอาร์เซไนด์สังเกตได้จากการเปล่งแสงของตัวอย่างเมื่อได้รับการกระตุ้นจากแสง (photoluminescence spectra) ที่อุณหภูมิ 20-100 เคลวิน อย่างไรก็ตามค่าความเข้มของแสงที่ได้ยังมีค่าไม่มากนัก เนื่องจากความหนาแน่นของจำนวนโครงสร้างวงแหวนอินเดียมแกลเลียมอาร์เซไนด์ที่ต่ำ ($\sim 10^{8}$ cm^{-2}) ทั้งนี้ ได้มีการแปรค่าตัวแปรในการวัดคุณสมบัติทางแสงอันประกอบไปด้วย ค่าความเข้มแสงที่ใช้ในการกระตุ้น อุณหภูมิในการวัด และโพลาไรเซชั่น พบว่าผลทางแสงที่ถูกโพลาไรซ์ของชิ้นงานตัวอย่างบ่งบอกถึงความไม่สมมาตรของโครงสร้างนาโนรูปวงแหวน

ภาควิชา .....วิศวกรรมไฟฟ้า..... **ลายมือชื่อนิสิต** .....

สาขาวิชา .....วิศวกรรมไฟฟ้า..... **ลายมือชื่อ.ที่ปรึกษาวิทยานิพนธ์หลัก**.....

ปีการศึกษา .....2553..... **ลายมือชื่อ.ที่ปรึกษาวิทยานิพนธ์ร่วม** .....

ลายมือชื่อ.ที่ปรึกษาวิทยานิพนธ์ร่วม.....

5071864021 : MAJOR ELECTRICAL ENGINEERING
KEY WORD: InGaAs / GaAs / NANOSTRUCTURES / DROPLET / MOLECULAR BEAM EPITAXY / QUANTUM RING

NARAPORN PANKAOW : THE FABRICATION OF InGaAs RING-LIKE NANOSTRUCTURES BY DROPLET MOLECULAR BEAM EPITAXY. THESIS ADVISOR : ASSOC. PROF. SOMCHAI RATANATHAMMAPHAN, D.Eng., THESIS CO-ADVISORS : PROF. SOMSAK PANYAKEOW, D.Eng., PROF. CHARLES W. TU, Ph.D., 66 pp.

InGaAs ring-shaped nanostructures, or quantum rings (QRs), have been fabricated by droplet epitaxy using solid-source molecular beam epitaxy (MBE). The droplet forming conditions have been varied by changing the growth parameters including substrate temperature (T_s~120-300°C) during $In_{0.5}Ga_{0.5}$ deposition, $In_{0.5}Ga_{0.5}$ deposited amount (2-5ML), and In-mole-fraction (x~0.3-0.7) of InGa droplets. The morphology of the QRs was characterized by atomic force microscopy (AFM). The effects of each growth parameters on the InGaAs QRs are investigated. Increasing T_s results in the InGaAs QRs of a larger size but lower density due to 2-dimensional expansion and merging of InGa droplets. Furthermore, increasing $In_{0.5}Ga_{0.5}$ amount deposited results in larger QRs at low T_s. However, the QR density oscillates with increasing $In_{0.5}Ga_{0.5}$ amount due to merging of small droplets into a full-layer. At higher T_s, increasing $In_{0.5}Ga_{0.5}$ amount results in the QRs of a higher height, higher density but smaller diameter due to the accumulating compressive strain inside larger QRs and the partial relaxation. Moreover, varying In-mole-fraction (x) of In_xGa_{1-x} droplets lead to a variation of crystallized-QR size and density, i.e.; high density tiny-size QRs from high-Ga-content droplets and low density large-size QRs from high-In-content droplets. For photoluminescence (PL) measurement, another set of samples were grown under the droplet forming conditions of 2-5 ML $In_{0.5}Ga_{0.5}$ deposition at 210°C, with an additional 100-nm GaAs capping layer grown by migration-enhanced epitaxy and conventional method. The optical properties of the InGaAs QRs were analyzed by PL spectra of the respective samples at 20-100 K. The PL intensity is relatively low due to low density of the QRs (~10^8 cm^{-2}). The PL measuring parameters, including excitation intensity, measuring temperature and polarization have been varied. When increase the excitation intensity, the PL intensities increase without shifting, indicating the ground-state energy of the InGaAs QR systems. With increasing the measuring temperature, the PL intensities decrease without thermal broadening. It is also observed that the spectra of 3 ML sample are not shifted. However, the spectra of 4 ML sample are red-shifted, implying the existence of the strain field. Finally, the polarized PL spectra correspond to the elongation of the QRs, confirming the anisotropy of the QRs.

Department ...Electrical Engineering... **Student's signature** .....
Field of study .Electrical Engineering.. **Advisor's signature** .....
Academic year .....2010..... **Co-advisor's signature** .....
Co-advisor's signature .....

Acknowledgements

The author would like to give special thanks to his family for endless and encouraging support throughout this work.

The author gratefully acknowledges all those who provided invaluable help and encouragement during the research at the Semiconductor Device Research Laboratory (SDRL), Department of Electrical Engineering, Faculty of Engineering, Chulalongkorn University, Bangkok, Thailand. In particular, the author would like to acknowledge Associate Professor Dr. Somchai Ratanathammaphan, Professor Dr. Somsak Panyakeow, and Professor Dr. Charles W. Tu who are the advisor and co-advisors. The author also would like to thank Lecturer Boonchuay Supmonchai, Assistant Professor Dr. Tara Cholapranee, and Associate Professor Dr. Twittie Senivongse for their advice on English grammar. Moreover, this research is financially supported by the Thailand Research Fund (TRF) through the Royal Golden Jubilee Ph.D. Program (Grant no. PHD/0011/2550) to Naraporn Pankaow and Somchai Ratanathammaphan. This research is also supported by Nanotechnology Center of Thailand (Nanotec), the Higher Education Research Promotion and National Research University Project of Thailand - Office of the Higher Education Commission (EN264A), Asian Office of Aerospace Research and Development (AOARD), and Chulalongkorn University. Finally, this thesis could not be completed without special helps of the SDRL researchers: Mr. Supachok Thainoi, Mr. Pronchai Changmaung, Mr. Poonyaseri Boonpeng, Mr. Ong-arj Tangmettajittakul, Dr. Wipakorn Jewasuwan, and colleagues.

CONTENTS

Page

LIST OF FIGURES

Figure Page

Figure Page

Figure Page

Figure Page

Figure Page

LIST OF SYMBOLS

∇^2	Laplacian operator
α	fitting parameter
AFM	atomic force microscopy
Al	aluminium
AlAs	aluminium arsenide
AlP	aluminium phosphide
As	arsenic
BEP	beam equivalent pressure
δ	delta function
Δ	total spectrum broadening from all excited quantum dot
$\Delta\gamma$	change of surface free energy
$D_{QD}(E)$	quantum dot density of state
D.O.S.	density of state
ε_0	lattice mismatch
E	carrier energy
	or total energy per unit cell
E_g	band gap energy
$E_{n,x}$	quantized energy in x-direction
$E_{n,y}$	quantized energy in y-direction
$E_{n,z}$	quantized energy in z-direction
F	free energy
$F(\mathbf{r})$	envelope wave function
FM	Frank van der Merwe
FWHM	full width at half maximum
γ_F	surface free energy of the grown film/vacuum interface
$\gamma_{F/S}$	interface energy between grown film and substrate
γ_S	surface free energy of the substrate/vacuum interface
g^{sat}	maximum optical gain
Ga	gallium
GaAs	gallium arsenide
GaP	gallium phosphide

h	Planck's constant
$\hbar$	reduced Planck's constant
$I(\Phi)$	persistent current of a quantum ring
$I(T)$	activation energy of potential wells
In	indium
InAs	indium arsenide
InGaAs	indium gallium arsenide
InGaP	indium gallium phosphide
InP	indium phosphide
k	Boltzmann's constant
k_B	Boltzmann's constant
$\lambda_{\text{de Broglie}}$	de Broglie wavelength
$l_{C\text{-}QD}$	distance between two adjacent coupled quantum dots
l_b	center barrier width
l_w	potential well width
L	macroscopic length scale
L_x	nanometer length scale in x direction
L_y	nanometer length scale in y direction
L_z	nanometer length scale in z direction
m^*	effective mass
MBE	molecular beam epitaxy
ML	monolayer
Mo	molybdenum
n	quantum number in z-direction (integer)
N_2	nitrogen
N_D	volume density of quantum dot
N_e	number of state per unit surface
p	carrier momentum
PBN	pyrolytic boron nitride
PL	photoluminescence
QD	quantum dot
QDM	quantum dot molecule
QR	quantum ring
RHEED	reflection high-electron energy diffraction

Si	silicon
SiGe	silicon germanium
SK	Stranski Krastanow
T	temperature
	or PL measuring temperature
T_s	temperature during $In_{0.5}Ga_{0.5}$ deposition
UHV	ultra high vacuum
$V(\mathbf{r})$	confinement potential function
VM	Volmer Weber
WL	wetting layer
Φ	magnetic flux piercing a ring
θ	angle
	or coverage

CHAPTER I

INTRODUCTION

1.1 Motivation

The techniques of self-assembled fabrication for nanostructures are highly attractive for basic physics and device applications. Useful for opto-electronics, the atom-like properties of quantum nanostructures such as carrier confinement and energy level quantization can lead to the emission of photon with a specific wavelength. For decades, various fabrication techniques for quantum nanostructures have been developed. In particular, the Stranski-Krastanov (SK) growth mode, one of the most widely used methods for fabrication, is driven by the strain from lattice mismatch between the substrate and the overlayer [1]. However, the non-uniform strain distribution in the lattice-mismatched system can affect the energy band structures, undesirable for studies of the physics of semiconductor nanostructures. Another growth technique that has been applied to form nanostructures without strain is droplet epitaxy technique [2-4]. This technique is simple and flexible. The droplet epitaxy process is simply based on the formation of the group III element droplets by depositing group III atoms on a crystalline surface, followed by a reaction with a group V element for crystallization into III-V compound nanostructures. The lattice-matched system in droplet formation can eliminate the strain energy and its effects on the energy-band structures. Moreover, it does not require additional complicated processing and has potential to develop the quantum nanostructures. Not only quantum dots (QDs) but also the complex nanostructures such as nanoholes [5,6], quantum rings (QRs) [2], and quantum dot molecules (QDMs) [7] have been demonstrated by this technique.

Among them, QRs, or ring-shaped nanostructures, are a special class of quantum-confinement structures. Just like QDs, QRs also have quantized energy levels due to their carrier confinement, which makes them potentially applicable in opto-electronics [8-10]. However, the QRs have attracted a lot of attention due to the additional features such as the Aharonov-Bohm effect [11,12]. One predicted feature of quantum rings is the magnetic properties which are related to the possibility of inducing persistent currents [12]. The QRs have been demonstrated through several approaches

including thin GaAs layer capping of InAs QDs [13-18], post-growth annealing process [1,19], SK growth [20,21], and droplet epitaxy [2,22-27]. Most of the QRs have been demonstrated by forming a thin layer of GaAs on SK-grown InAs QDs (*Lorke et al. (2001); Granados et al. (2003); Kiravittaya et al. (2003); Schmidt et al. (2002); Songmuang et al. (2003); Garc et al. (1997)*). The formation mechanism is driven by the reduction of the surface free energy around InAs QDs due to the deposition of a thin GaAs layer. After the short annealing, a remarkable morphological change results in QR formation.

While many of the approaches utilize the conversion of QDs to QRs, the droplet epitaxy technique can form QRs directly. In past years, there are experimental results reported in literatures about QRs grown by droplet epitaxy [2,5,6,22-24,26,28]. Most are the fabrication of GaAs QRs in GaAs/(Al)GaAs material systems. *Mano et al. (2005) and Lee et al. (2006)* have proposed the evolution of lattice-matched GaAs/$Al_{0.3}Ga_{0.7}As$ QRs grown by droplet epitaxy. The growth simply starts with the formation of Ga droplets on $Al_{0.3}Ga_{0.7}As$ surface and then follows by crystallization in As_4. During the crystallization, Ga droplets interact with As atoms and change to GaAs QRs. The high structural and optical qualities of the QRs are confirmed. Furthermore, *Alonso-Gonzalez et al. (2007)* demonstrated the formation of InAs QDs in a low-density template of GaAs/GaAs QRs fabricated by droplet epitaxy. By capping the template with 1.4 ML conventional InAs, InAs QDs are restrictively formed only inside the template QRs. With use of this low-density strain-free template, the low-density InAs QDs (~10^8 cm^{-2}) can be realized. By the way, In(Ga)As/GaAs is another interesting systems due to exhibited quantum confinement. Recently, there are several literatures about InAs/GaAs QRs grown by droplet epitaxy. *Noda et al. (2008) and Lee et al. (2008)* have reported the fabrication of InAs QRs on GaAs (100) by droplet epitaxy. Diameter and Density of the resulted QRs are ~ 200-400 nm and ~ 10^6 cm^{-2}, respectively. Very low density and relatively large size of such QRs still be a limitation of InAs/GaAs QR formation and undesirable for optical application. This is resulted from a too long 2-dimentional surface migration length of In atoms and high segregation effect of newly supplied adatoms. A solution to overcome the problems is the growth at low temperature with an optimum crystallization [29]. Another solution is to limit the migration length of In atoms on GaAs. Ga is also supplied together with the deposition of In. Predictedly, the structural properties of crystallized InGaAs QRs are different from pure-InAs QRs. Moreover, it's clear that the QRs are originated from the

respective droplets, so changing of droplet forming condition subjects to vary the properties of the crystallized QRs. Hence, a clear demonstration of the formation of InGaAs QRs by droplet epitaxy is desirable.

In this dissertation, the formation of low-density InGaAs ring-like nanostructures (QRs) on GaAs (100) by droplet epitaxy technique using MBE was demonstrated. The evolution of morphology and the formation mechanism have been investigated. The droplet-forming conditions have been varied by changing the growth parameters including substrate temperature during depositing InGa (T_s), $In_{0.5}Ga_{0.5}$ amount, and Indium-mole-fraction. The surface morphology of the QRs was analyzed by using an atomic force microscope (AFM). The effects of the growth parameters on the InGaAs ring-like nanostructures grown by droplet epitaxy were also investigated. For photoluminescence (PL) measurement, the InGaAs QRs were repeatedly grown under several selected droplet-forming conditions with an additional 100-nm GaAs capping layer. PL measurement was performed to characterize the optical properties of the InGaAs QRs.

1.2 Objectives

This dissertation objective is to demonstrate the fabrication of InGaAs ring-like nanostructures, so called quantum rings (QRs), on GaAs by droplet epitaxy technique using molecular beam epitaxy. The growth parameters including 1) substrate temperature during the deposition (T_s), 2) deposited $In_{0.5}Ga_{0.5}$ amount, and 3) Indium-mole-fraction (x) of In_xGa_{1-x} have been varied. The effects of growth parameters on the morphological properties of the InGaAs QRs (QR size and density) have been analyzed through the surface morphology of the InGaAs QRs grown with different growth conditions. Also, the optical properties of the InGaAs QRs have been investigated from PL spectra of the 100-nm-GaAs capped samples at 20-100 K.

1.3 Overview

This dissertation presents a detailed study of the fabrication of InGaAs ring-like nanostructures by droplet epitaxy technique using molecular beam epitaxy (MBE). The purpose is to analyze the effects of droplet forming parameters on the structural and optical properties of the nanostructures.

The thesis is organized as follows: The basic concepts are reviewed in chapter 2. This also includes fabrication techniques for nanostructure formation. Chapter 3 gives the experimental details. Moreover, the information of the equipments used in this work is briefly introduced. In chapter 4, the experimental results from the fabrication of InGaAs QRs are presented. Also, the evolution of surface morphology by RHEED observation and predicted QR-formation mechanism are represented. The effects of substrate temperature during $In_{0.5}Ga_{0.5}$ deposition, $In_{0.5}Ga_{0.5}$ amount deposited, and Indium-mole-fraction of droplets on the morphological and optical properties of InGaAs QRs are studied in this chapter. The studies are based on atomic force microscopy (AFM) and photoluminescence (PL) results. Finally, chapter 5 concludes this work.

CHAPTER II

RATIONALE, THEORY AND HYPOTHESIS

The basic concepts of quantum dot (QD) structure, which is a low-dimensional semiconductor nanostructure, are reviewed in this chapter. A comparison of important intrinsic properties of nanostructures is presented. The properties of quantum rings (QRs), a type of quantum-confinement structures, are also reviewed to be useful for the interpretation of nanostructure characteristics.

In another part of this chapter, self-assembled growth of the nanostructures is presented based on epitaxial growth. Self-assembled growth modes are briefly introduced to provide the basics of nanostructure formation from strain-releasing in a lattice mismatch system. The next section, a review of droplet epitaxy which is the lattice-matched method used to fabricate the QRs in this research work is presented. Migration-enhanced epitaxy (MEE) is also briefly introduced. Finally, the information of the material system which is used to create the nanostructures is provided.

2.1 Quantum Nanostructures

The electronic properties for quantum dot (QD) structures differ from the bulk system. While the bulk has a continuous energy band, the low-dimensional nanostructures have discrete energy levels and delta-like density of states due to the carrier confinement and quantization of carrier energy. Hence QD is also called an *artificial atom* for its quantized energy levels like a real atom.

2.1.1 Carrier confinement and energy level quantization

The band theory of crystals has been rigorously developed from the quantum theory for atoms since the last century [30,31]. Figure 2.1 shows a schematic comparison between a bulk semiconductor, a waveguide for visible light, a QD, and an atom. From the quantum theory, we know that an atom has discrete energy levels. Atoms together would become a solid with energy bands. The most relevant bands are the conduction band and the valence band which are separated in energy by the band

gap. At T = 0 K, the conduction band is free of electrons while the valence band is full with electron. At $T > 0$ K, these two bands are partially filled with electrons and holes (carriers in device operations). Controlling the *carrier motion* in these two bands is the subject of band gap engineering.

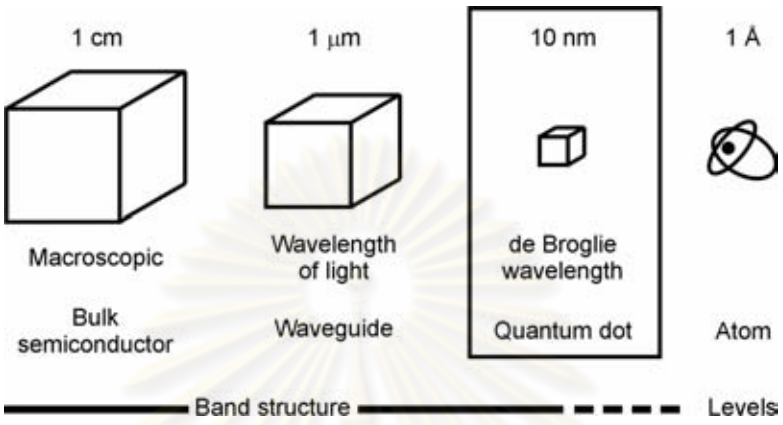

Figure 2.1 Schematic comparison of bulk, waveguide, QD, and atom [32].

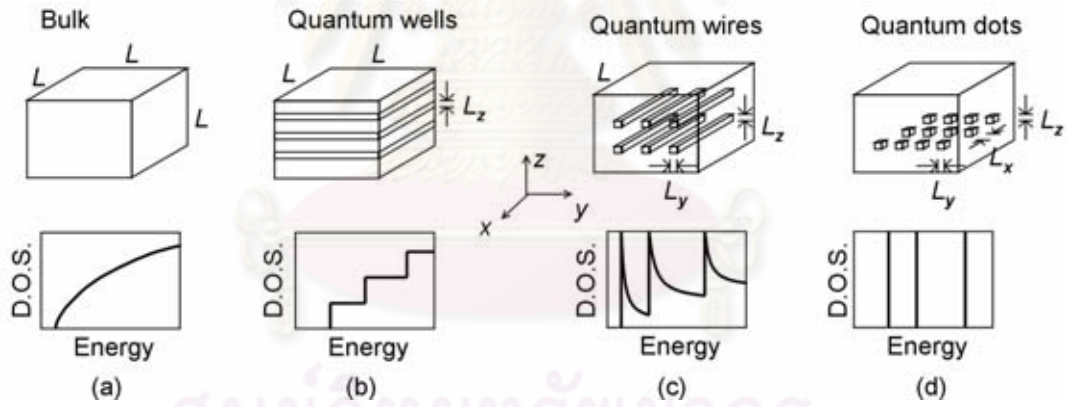

Figure 2.2 Schematic views and graphs of (a) bulk (3-D structure), (b) quantum wells (2-D structure), (c) quantum wires (1-D structure), and (d) QD (0-D structure) and their density of states (D.O.S.) [33]. L is in macroscopic scale (~cm), while L_x, L_y, L_z, are in nanoscale.

Because the structural size is varied continuously, there exists a description between the two cases (discrete levels and continuous band structure). The densities of states of energy band structure of bulk semiconductor and low-dimensional nanostructures are illustrated in figure 2.2 [33]. In the case of QD, since the low-

dimensional-shaped nanostructures provide the potential well resulted from difference of energy band gap (E_g) of 2 materials in the three directions, the carrier motions are completely confined in this 3-D confinement structure and result in a delta function density of states. The specific energy photons would be emitted when the nanostructures are stimulated.

The quantization phenomenon can be described by wave-like properties of confined electrons, since any substance would exhibit its related wave properties. In the low-dimensional nanostructures, most of carriers are confined in one or more directions and the length scale of confining direction is in the order of the de Broglie wavelength (carrier wavelength). The de Broglie wavelength, $\lambda_{\text{de Broglie}}$, depends on the carrier effective mass, m^*, and temperature, T [34]:

$$\lambda_{\text{de Broglie}} = \frac{h}{p} = \frac{h}{\sqrt{3m^* k_B T}} \tag{2.1}$$

where h is Planck's constant, p is carrier momentum, and k_B is Boltzmann's constant.

In a potential well, the confined carriers are limited in their motion, so they look-like stationary. The wave-like properties of a *stationary* electron can be only de Broglie wavelengths which create standing wave within the width of the potential well, that is, the width of the nanostructures. The discrete-values of carrier's de Broglie wavelengths would be exhibited, and cause discrete energy levels in such 3-D confinement structures. A schematic representation of the lowest three levels of carrier energy quantization in a potential well is shown in figure 2.3.

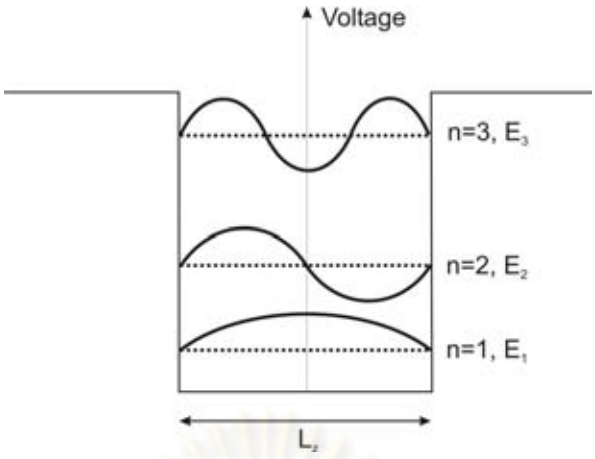

Figure 2.3 The lowest three levels of carrier's energy quantization in a potential well with a width of L_z (comparable to de Broglie wavelength). The picture shows examples of the three lowest-energy standing waves (solid line) which can happen in a potential well and the corresponding carrier's energy level of the de Broglie wavelength from the standing wave (dotted line), i.e. E_1, E_2 and E_3. The energy of each level is given by $E_{n,z} = \hbar^2 (n\pi)^2 / 2m^* L_z^2$, where *n* is an integer number.

In semiconductor quantum structures, the effective-mass approximation is widely used for the quantized energy level calculation as a function of the well width [35]. The main assumption of the effective-mass approximation is that the envelope wave function does not significantly vary in the unit cell with a length scale of subnanometers, therefore this assumption is valid in all low-dimensional nanostructures. Assuming parabolic band dispersion, the band-edge electron states of semiconductors can be described by a Schrödinger-like equation as

$$\left[-\frac{\hbar^2}{2m^*} \nabla^2 + V(\mathbf{r}) \right] F(\mathbf{r}) = E\, F(\mathbf{r}) \qquad (2.2)$$

Here, m^* is the effective mass; $\hbar$ is the reduced Planck's constant; $\mathbf{r} = (x,y,z)$ is the carrier position vector; $V(\mathbf{r})$ is the confinement potential due to band offset. $F(\mathbf{r})$ is the envelope wave function; and E is the carrier energy.

From eq. (2.2), by assuming the barrier potentials with *infinite height*, the carrier energy E and density of states per unit volume (D.O.S.) (the number of states

between the energy E and $E + dE$, of each quantum nanostructure) in the case of QD can be written as follows [33],

Assuming that the infinite confinement potential barrier in all direction, we get [33]

$$E_{\mathrm{QD}} = E_{n_x} + E_{n_y} + E_{n_z} = \frac{\hbar^2}{2m^*}\left[\left(\frac{n_x\pi}{L_x}\right)^2 + \left(\frac{n_y\pi}{L_y}\right)^2 + \left(\frac{n_z\pi}{L_z}\right)^2\right] \tag{2.3}$$

$$D_{\mathrm{QD}}(E) = 2N_D \sum_{n_x,n_y,n_z} \delta(E - E_{n_x} - E_{n_y} - E_{n_z}) \tag{2.4}$$

where δ is the delta function, and N_D is the volume density of QD.

The change of density of states for the low-dimensional nanostructures (figure 2.2) affects the fundamental properties of devices, which use these nanostructures as an active layer [36]. In the case of QD structures, there are several theoretical and experimental proofs that semiconductor lasers consisting of QD structures have the lowest threshold current density due to the delta-function-like density of states [37].

To utilize QDs as an active layer for semiconductor laser applications, the maximum optical gain (g^{sat}) for a QD laser should be considered [38];

$$g^{sat} \propto N_e/\Delta \tag{2.5}$$

where N_e is the number of states per unit surface area and Δ is the total spectrum broadening from all excited QDs. From eq. (2.5), it's possible to increase g^{sat} by increasing the QD density (to increase N_e) and/or reducing the QD size distribution.

2.1.2 Double potential well

The coupling of double potential well is briefly discussed in *"Quantum Wells, Wires & Dots" (Paul Harrison, 2005)*, using an example of GaAs/$Ga_{1-x}Al_xAs$ double potential wells. The simplest example of the former would be the symmetric double well of Figure 2.4. The potential function V(z) required for the numerical solution is simply the conduction band edge as given in figure 2.4.

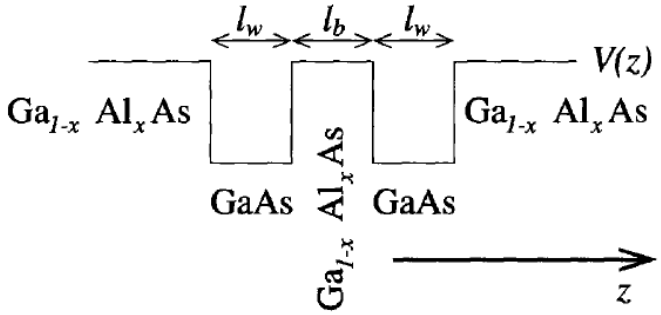

Figure 2.4 Band profile of symmetric GaAs/$Ga_{1-x}Al_xAs$ double potential well [39].

Figure 2.5 displays the results of calculations of the lowest two energy states as a function of the central barrier width for a double potential well with the Al barrier concentration x = 0.2 and a fixed well width l_w — 60 Å. When the wells are separated by a large distance, the interaction between the eigenstates localized within each well is very small and the wells behave as two independent single wells. However, as illustrated in Figure 2.5, as the central barrier l_b (corresponding to distance between two wells) is decreased, the energy levels interact, with one being forced to higher energies and the other to lower energies.

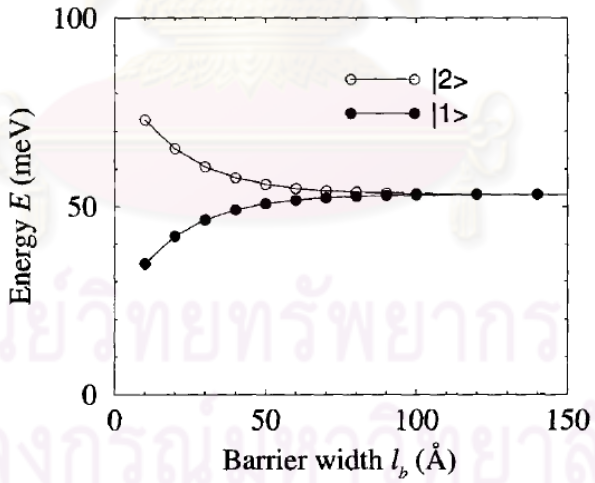

Figure 2.5 Confinement energies of the lowest two states of a symmetric double potential well as a function of the central barrier width [39].

In the case of the double potential well, a situation occurs with the electron spins aligning in an *anti-parallel* arrangement in order to satisfy the Pauli's exclusion principle. Figure 2.6 displays the wave functions of the double well with a central

barrier width of 40 Å. Clearly, they form a symmetric and anti-symmetric pair, with the former being of lower energy.

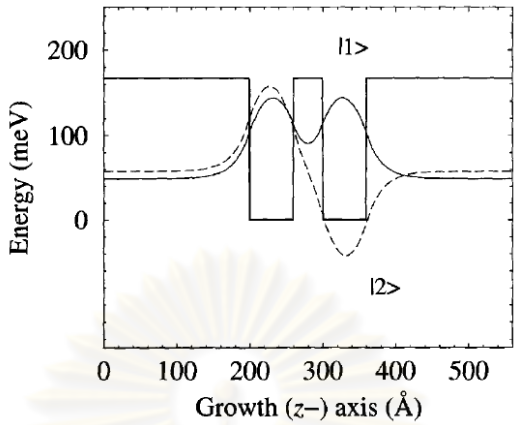

Figure 2.6 Wave functions of the lowest two energy levels of the symmetric double potential well with a central barrier width of 40 Å [39].

2.1.3 Ring-shaped nanostructures or quantum rings (QRs)

The ring-shaped nanostructures, so called quantum rings (QRs) are another type of quantum-confinement structure. Like QDs, QRs have their energy level quantized due to their confinement properties. This makes them potentially applicable in electronics, optics, and quantum information processing [8-10]. However, semiconductor quantum rings have attracted a great deal of attention because of their additional properties predicted and demonstrated [40,41]. For example, the ring-structures are a special class of quantum-confinement due to the Aharonov-Bohm effect, which is specific to the topology of a ring [42]. Also, interesting are magnetic properties of QRs, which are related to the possibility of inducing persistent current inside the structure when they are put into a magnetic field.

The persistent current of a quantum ring [43] can be written in general as

$$I(\Phi) = -\frac{\partial F}{\partial \Phi}, \tag{2.6}$$

where F is the free energy of the system and Φ the magnetic flux piercing the ring. At zero temperature, the free energy can be replaced with the ground state energy. The energy of a ring and consequently also the persistent current is a periodic function of

the flux. The effect of the magnetic field is to lower the energy states of high angular momentum with respect of those at low angular momentum [43]. When the flux is increased, the ground state energy will jump from one angular momentum to the next causing the periodic behavior.

2.1.4 Material Considerations

Mostly, the preliminary condition for the growth is that the nanostructure material has a smaller band gap compared with the matrix material(s) to provide a potential well in the energy band. Unlike the SK growth mode, the material for the nanostructure fabricated by droplet epitaxy does not necessarily have a larger or smaller lattice constant since the method can be applied to lattice-matched system such as AlGaAs/GaAs. Figure 2.7 shows the relationship between the band gap energy and the lattice constant of III-As material systems. There is a possibility to realize nanostructures which emit light at the wavelength of 1.3 μm or 1.55 μm (dashed lines).

For laser applications in optical communication systems, GaAs is the most important substrate material. The self-assembled growth of InGaAs on a GaAs substrate can provide the nanostructures which emit light at 1.3 μm or longer wavelength, depended on the ratio of In and Ga in the InGaAs structures. In this work, we shall concentrate only on the InGaAs/GaAs material system.

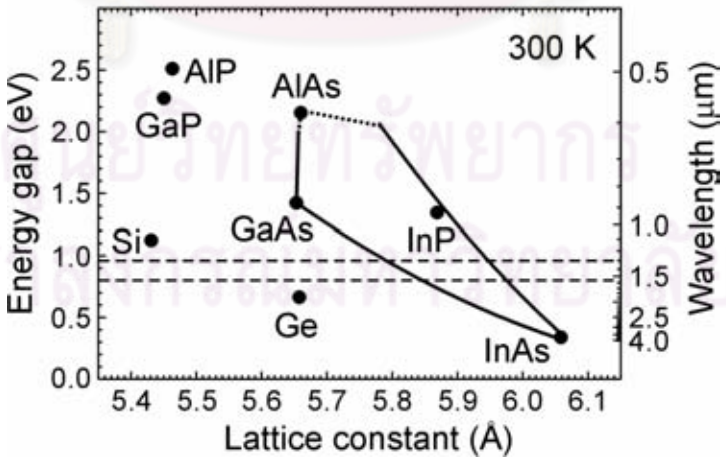

Figure 2.7 The relationship between lattice constant and energy gap at room temperature for the III-As material system. The solid line: direct band gap material, and the dotted line: indirect band gap material.

2.2 Self-assembled growth

The self-assembled growth can realize nanostructures such as QDs. The growth mode and growth conditions for self-assembled growth are briefly reviewed in order to provide some basic understanding of the growth method. Droplet epitaxy is also introduced as the fabrication technique used in this work.

2.2.1 Growth modes

To define the growth mode during the film deposition, $\Delta\gamma$ (the change of total energy of a surface before and after deposition) is considered:

$$\Delta\gamma = \gamma_F + \gamma_{S/F} - \gamma_S \tag{2.7}$$

where γ_S is substrate surface energy, γ_F is film surface energy, and $\gamma_{S/F}$ is interface energy between the grown film and the substrate including the additional energy arising from the strain between the film and the substrate.

If $\Delta\gamma > 0$, the deposited material would prefer to cover the substrate surface since the interaction between the substrate and deposited atoms is stronger than that between neighboring atoms. This is Frank Van der Merwe growth mode or layer-by-layer growth (figure 2.8(a)). If $\Delta\gamma < 0$, the interaction between the substrate and neighboring atoms exceeds the overlayer-substrate interaction, thus, the 3D Volmer Weber growth mode is observed (figure 2.8(c)).

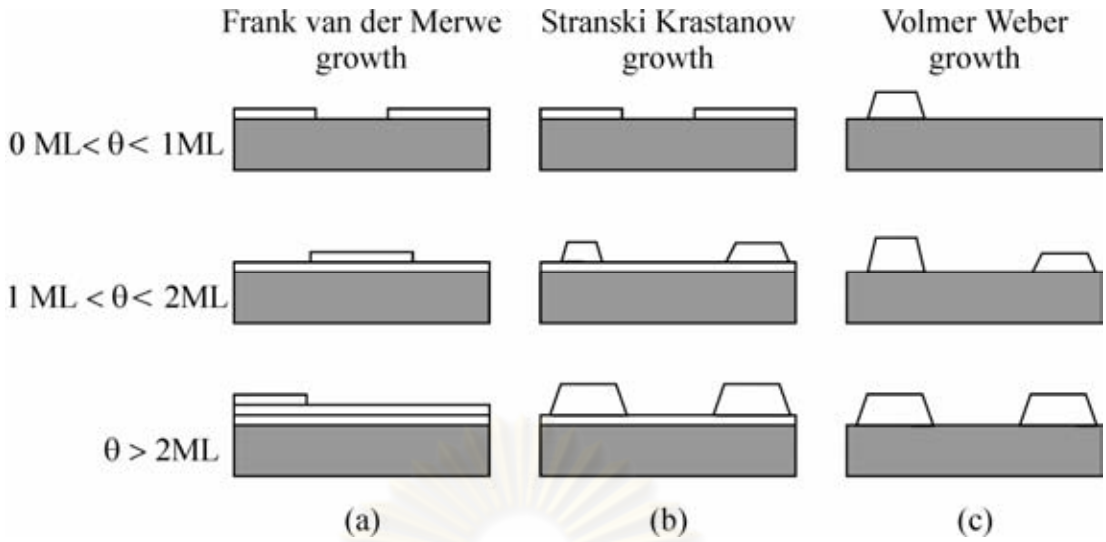

Figure 2.8 Schematic representation of the 3 important growth modes of a film for different coverage (θ) (a) Frank van der Merwe (FM), (b) Stranski Krastanow (SK), and (c) Volmer Weber (VM) [44].

In the intermediate case, the deposited film can grow a few monolayers in layer-by-layer growth mode at the early stage of deposition ($\Delta\gamma < 0$). However, due to the strain between the grown film and the substrate accumulating with the deposited film thickness, the islands are formed on top of the *intermediate* layer (the wetting layer (WL)) since $\Delta\gamma$ becomes less than zero and the growth mode changes from 2D-growth mode to 3D-growth mode. This is layer-plus-island growth in Stranski-Krastanov growth mode (Figure 2.8(b)) used in the growth of many conventional QDs [45,46].

Although this growth mode is not used to fabricate the nanostructures in this work, the detail of SK growth mode is briefly introduced to provide the basics of QD formation from strain-releasing in a lattice-mismatched system. The Stranski-Krastanow (SK) growth mode is widely used to fabricate defect-free self-assembled QD structures in the case of lattice-mismatched systems (lattice mismatch : $\varepsilon_0 > 7\%$). First, a few monolayers of strained material grow in the layer-by-layer growth mode. During the growth, the elastic strain energy builds up due to the lattice mismatch and increasing film thickness [47]. The island formation is energetically favorable if material beyond critical thickness is deposited, because the lattice can elastically relax compressive strain and thus reducing strain energy, as shown in figure 2.9. Beyond the critical thickness, the layer-by-layer growth is unfavorable so elastic strain relaxation

occurs. The local strain energy density of the SK-growth mode QD is schematically represented in figure 2.10.

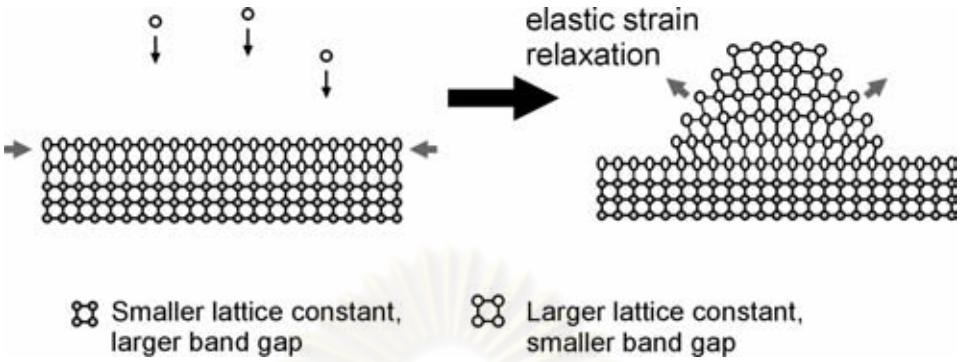

Figure 2.9 Illustration of island formation during epitaxial growth of a semiconductor material on the top of another semiconductor with a smaller lattice constant in Stranski-Krastanow mode.

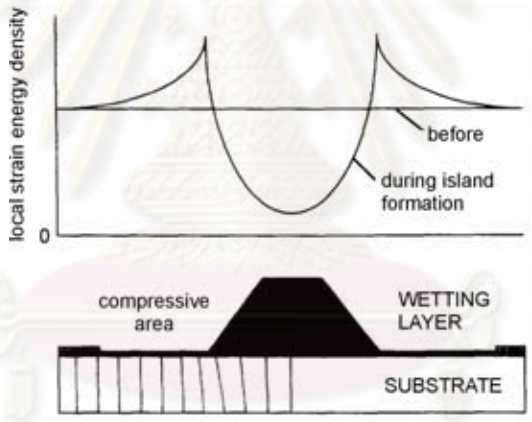

Figure 2.10 Schematic representation of the local strain energy density in and around the SK-growth mode QD. The energy barrier has a maximum at the edge of the QD [47].

Although the QDs grown by this technique form into high-density arrays. There are still some disadvantages of this technique. First, the SK growth mode QDs exhibit wide size distribution, varying the energy level in the energy band. Since, carriers in a small size QD would exhibit shorter de Broglie wavelength of which corresponding energy level is higher. The representations of the energy level exhibited in the QD with different size are shown in Figure 2.11. Also, the non-uniform strain

distribution from the lattice-mismatched formation would effect on the energy band structure of QD [48]. Both are undesirable for the laser applications.

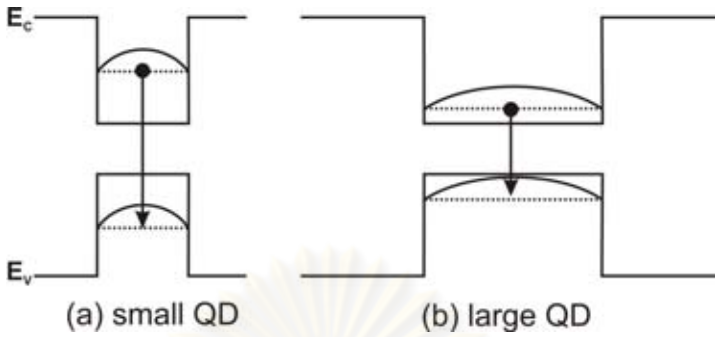

Figure 2.11 Simple interpretation of the energy level exhibited in the QD with different size. The representations in case of (a) small QD show the higher energy level than that of large QD, (b) due to the carrier confinement properties.

2.2.2 Droplet Epitaxy

Droplet epitaxy is an alternative approach of self-organized nanostructure fabrication which can be applied to both lattice-matched [22,49-52] and mismatched system. Unlike SK growth mode, the nanostructures fabricated by droplet epitaxy are originated directly from strain-free group III-element droplets formed on a crystalline III-V surface instead of strain-releasing in a lattice-mismatched system. Therefore, the strain-energy in the nanostructure and its effects on the energy-band structure are reduced due to the lattice-matched droplet formation. Thus, high-quality strain-less nanostructures can be fabricated by this technique, useful for the studies of semiconductor QR physics.

The droplet epitaxy process consists of 2 main steps. The illustration of the nanostructure fabrication by droplet epitaxy is shown in figure 2.12. First, group III metallic droplets are formed on a III-V compound substrate surface by depositing group III atoms on the substrate under the absence of group V. The formation mechanism of group III metallic droplets is explained by Volmer-Weber growth mode [44], in which the bonding energy between incoming group III adatoms is much higher than the bonding energy between the surface and the adatoms. Therefore, as soon as incidenting III-V surface, liquid In and Ga coalesce and form hemispherical droplets

(instead of layers). Second, the group III droplets are crystallized in group V molecular beam to form III-V compound nanostructures.

Since the III-V nanostructures are originated from respective droplets, the structural properties of the III-V compound nanostructures can be controlled by droplet forming parameters, such as substrate temperatures and amount of group III-element deposited. Since the droplet properties are still metallic, their morphology can be varied by changing such parameters. The crystallization conditions also affect the nanostructures.

However, there are limitations for the fabrication of InAs nanostructures on GaAs by droplet epitaxy such as very low density (~10^7-10^8 QRs/cm^2) and large size (~200-400 nm) [3,24] due to a too long 2-D migration length of In and high segregation effect of the newly supplied adatoms. To overcome these problems, the growth should be done at low temperature and use the optimum crystallization conditions [29]. Another solution is to limit the migration length of In atoms on a GaAs surface. Ga is also supplied together with the In deposition [53] and form InGa droplets. InGaAs nanostructures are formed after the crystallization.

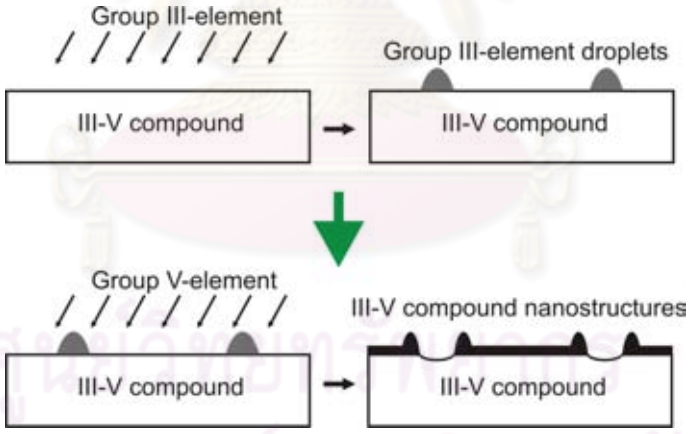

Figure 2.12 The illustration of the nanostructure fabricated by droplet epitaxy.

2.2.3 Migration-Enhanced Epitaxy (MEE)

Migration-enhanced epitaxy (MEE) of III-V compound semiconductors is useful for growing high quality epitaxial layers even at low substrate temperature (300°C-400°C). Unlike the conventional growth, the MEE growth proceeds in a layer-by-layer manner, based on alternately supplying group III atoms and group V to III-V

surface to obtain metal-stabilized surfaces, periodically. The shutter operation of MEE is shown in figure 2.13. In the growth of III-V compound semiconductors, the surface migration is effectively enhanced by supplying group III atoms to the growing surface in the absence of group V. Since, when the number of group III atoms supplied to the surface is much less than the number of surface sites, these atoms are quite mobile in the surface and do not cohere with each other to the surface site number. As a result, the lifetime of isolated group III atoms is greatly increased, resulting in these atoms migrating in a large distance along the surface, even at low temperature [44,54].

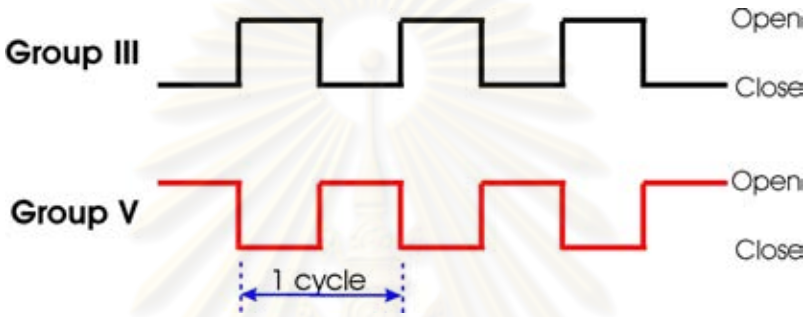

Figure 2.13 Shutter operation characteristic of migration-enhanced epitaxy (MEE).

CHAPTER III

EXPERIMENTAL DETAILS

In this chapter, the sample fabrication processes by droplet epitaxy technique are described in details. The growth equipment, molecular beam epitaxy (MBE), is introduced. In situ reflection high-electron energy diffraction (RHEED) installed with this MBE system is used to calibrate the growth rate and observe the evolution of surface structure during the growth. Also, ex situ characterizing-techniques including atomic force microscopy (AFM) and photoluminescence (PL) spectroscopy are introduced.

3.1 Molecular Beam Epitaxy

Molecular beam epitaxy (MBE) is a popular technique for growing III-V compound semiconductors. With a clean and ultra high vacuum (UHV) environment, the molecular beams of the constituent elements are incident upon a heated crystalline substrate and produce high-quality layers with very abrupt interfaces. It also has good control of thickness, doping, and composition, because of very low growth rate (monolayer (ML)/s), and the precise control of beam fluxes and growth conditions on an atomic scale. Quantum devices with high efficiency, high speed and high performance can be demonstrated. It can be said that MBE-grown quantum well structures closely approximate the idealized square-well potential models used in solid state theory.

In this research, a solid-source conventional RIBER 32P MBE machine consisting of three UHV chamber modules, i.e., introduction chamber, transfer chamber, and growth chamber, is used to fabricate the samples. Three chambers are separated by isolation gate valves. The pumping system including ion pumps, and titanium sublimation pumps are installed to keep UHV condition. A figure of RIBER 32P MBE is shown in Figure 3.1. The pressure of each chamber is measured by an ionization gauge. Epitaxial growth is done in the growth chamber cooled by liquid N_2 to keep base pressure below ~ 1×10^{-10} Torr. The manipulator with the substrate is rotated continuously during the growth to provide a uniform flux profile on the substrate

surface. The group III-elements (i.e. In, Ga, and Al) and group V-elements (i.e. As_4) are contained in pyrolytic boron nitride (PBN) crucibles which are installed in a separated effusion cells. Each cell is heated by its own heater the temperature of which is controlled by feedback from a standard thermocouple to a computer. The molecular beam flux of each element is controlled by a tantalum shutter in the front of each cell. A schematic drawing of the modified III-V MBE growth chamber is shown in Figure 3.2.

The unique advantage of MBE from other techniques is to study and control the growth process in situ. In particular, reflection high energy electron diffraction (RHEED) allows directly monitoring the surface structure of the sample and the already grown epilayer. The explanation on RHEED is presented in the next section. In addition, quadrapole mass spectroscopy is also used for particle analysis in the growth chamber.

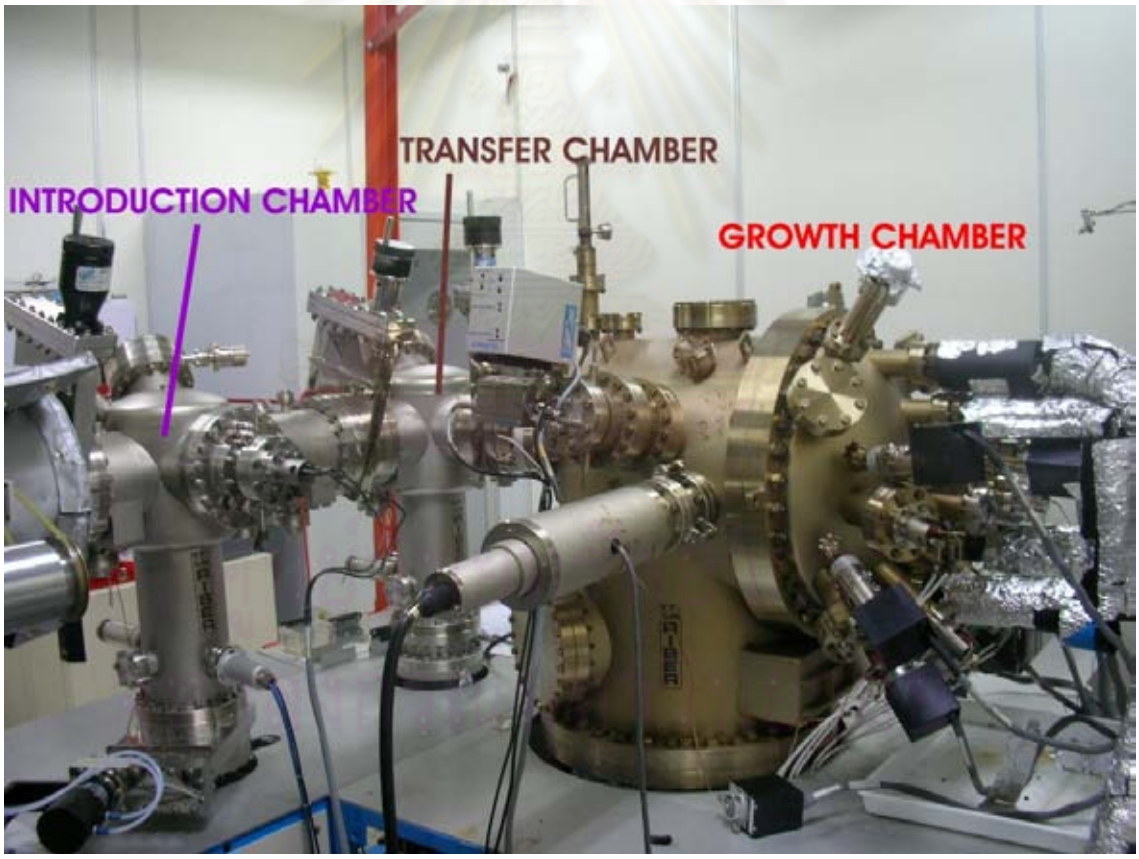

Figure 3.1 The conventional RIBER 32P MBE.

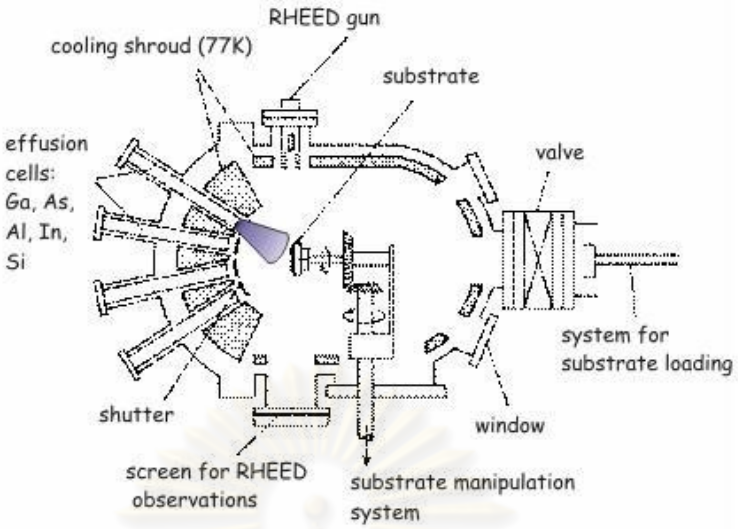

Figure 3.2 Schematic drawing of the modified III-V MBE growth chamber. The chamber is cooled by liquid N_2 (the base pressure < 1×10^{-10} torr).

3.2 Reflection High Energy Electron Diffraction (RHEED)

Reflection high energy electron diffraction is an in situ technique for characterizing thin films. It allows direct monitoring of the surface structure of the sample and already grown epilayer. It also allows observation on the dynamics of the growth. A schematic representation of a RHEED system is shown in Figure 3.3. A high-energy electron beam (~15 keV) intersects with the sample surface at a small angle (θ ~1-3^o). It is diffracted by the surface atoms, which function as a grating. The scattered electrons interfere constructively and form a pattern on the fluorescent screen. The RHEED pattern is captured with a high-performance CCD camera and analyzed by the data processing software installed in the computer.

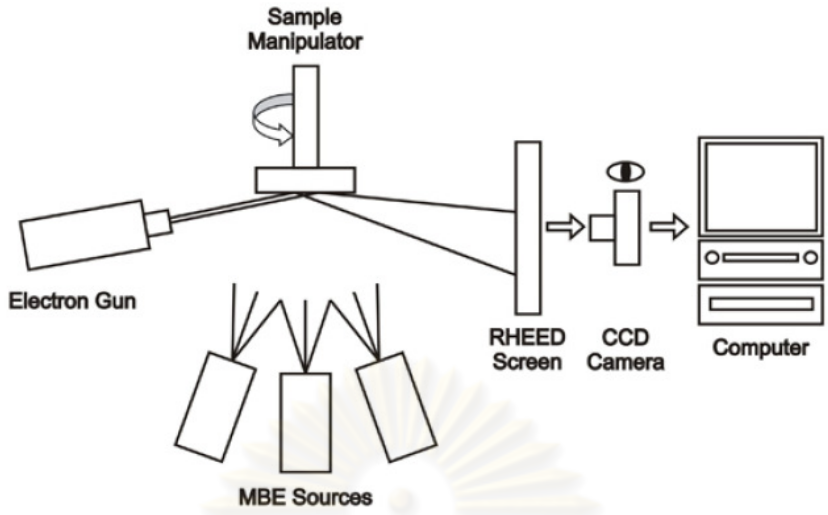

Figure 3.3 Schematic representation of RHEED system.

The pattern position can be graphically determined by the Laue method – intersection of Edwald sphere in the reciprocal lattice space. A schematic representation of RHEED observation is illustrated in Figure 3.4. Since the short de Broglie wavelength of electrons allows a shallow penetration depth into the substrate, the electron beam samples the topmost atomic layers. The diffracted electrons at the flat surface are imaged onto the screen. Therefore, the surface layer is represented by a reciprocal lattice space rod perpendicular to the real surface [44]. If the surface has roughness in the order of an atomic scale, the surface layer in the reciprocal space will be presented by three-dimensional point array. Therefore, we can interpret the RHEED pattern as the reciprocal lattice representation of the sample surface, which reflects the surface morphology on the atomic scale.

In this work, in situ RHEED observation is used to monitor surface structures during the growth of GaAs buffer layer and during the growth of nanostructures.

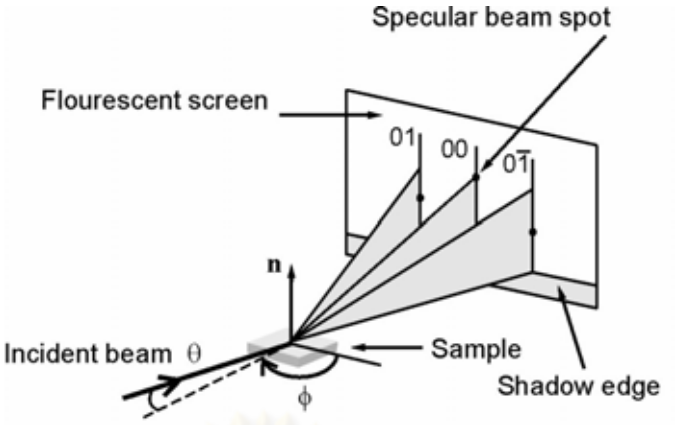

Figure 3.4 Schematic diagram of RHEED geometry of the incident electron beam at an angle θ to the surface plane [44].

3.2.1 RHEED intensity oscillation

The growth rates also can be determined by using RHEED intensity oscillations. The intensity oscillations are used to calibrate group III beam fluxes corresponding to the growth rate. To control the alloy composition and the thickness of quantum structures grown, the fluxes are adjusted to the value corresponding to needed growth rate [44].

The RHEED intensity on the pattern depends on the roughness of the surface. Under the normal growth conditions, the RHEED intensity, i.e., surface roughness, changes according to the fraction of surface coverage where a period of the pattern oscillation corresponds to the growth of 1 monolayer (ML). A schematic representation of the RHEED intensity oscillations is shown in Figure 3.5. In each period, the maximum reflectivity occurs at the initial and final state with a completed smooth surface and the minimum reflectivity occurs at the intermediate state when the grown layer is approximately half completed. With use of the period of oscillation signal, the growth rate of GaAs and others can be calibrated too.

Figure 3.5 Schematic representation of RHEED intensity oscillations related to formation of the first two completed monolayer of GaAs (001) [44].

3.3 Atomic Force Microscopy (AFM)

Atomic force microscopy (AFM) is a very powerful microscopic technique, a demonstrated resolution of fractions of a nanometer. A schematic representation of an AFM system is shown in Figure 3.6. The AFM scanning module consists of a cantilever

with a sharp silicon or silicon nitride tip, the size of which is in the order of nanometers at its end. The tip is brought into close proximity of a sample surface and scan through out the selected area. Typically, the deflection is measured by a laser spot reflected from the metal coated top of the cantilever into an array of photodiodes and digitally processed. A schematic representation of AFM measuring modes is shown in Figure 3.7. In this work, the AFM is operated in the tapping mode to reduce the friction during the measurement.

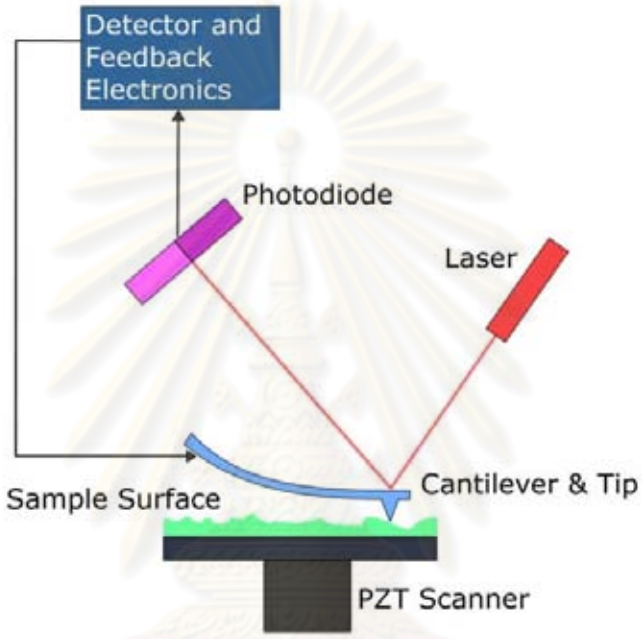

Figure 3.6 Schematic drawing of Atomic Force Microscopy (Drawn October 12, 2002 by Allen Timothy Chang).

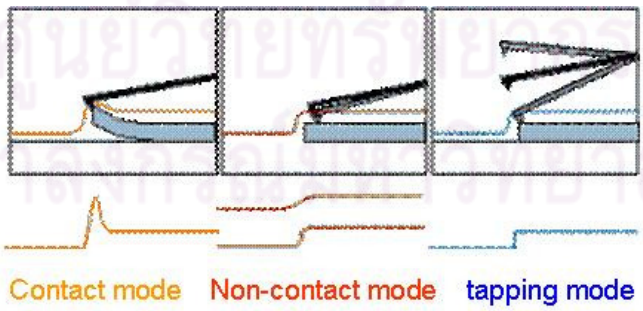

Figure 3.7 The schematic representation of AFM measuring modes including contact mode, non-contact mode and tapping mode.

In this work, the AFM images are performed by using a SEIKO SPA 400-AFM. The AFM is operated in the tapping mode in order to reduce the friction during the measurement. The scan rate is about 1-2 Hz (line per second) and the scan size is usually 1×1 - 5×5 μm^2 with 512 data points per scan line.

3.4 Photoluminescence (PL) Measurement

Photoluminescence (PL) spectroscopy is a technique for characterizing the optical properties of a sample through its luminescence. A schematic of the PL experimental setup is shown in Figure 3.8. The samples are excited by the 478-nm line of an Ar^+ laser. The laser beam is chopped and focused to the sample by focal lens. The light signal is analyzed by using a monochromator. A high-pass filter is used to filter the visible-light noise and the reflected laser beam signal. Then, the resolved light is detected by a liquid-Nitrogen-cooled InGaAs detector. A chopper and a lock-in amplifier are used to enhance the signal by the standard lock-in technique. The polarizer is installed to the system when we characterize the polarization of the QR systems.

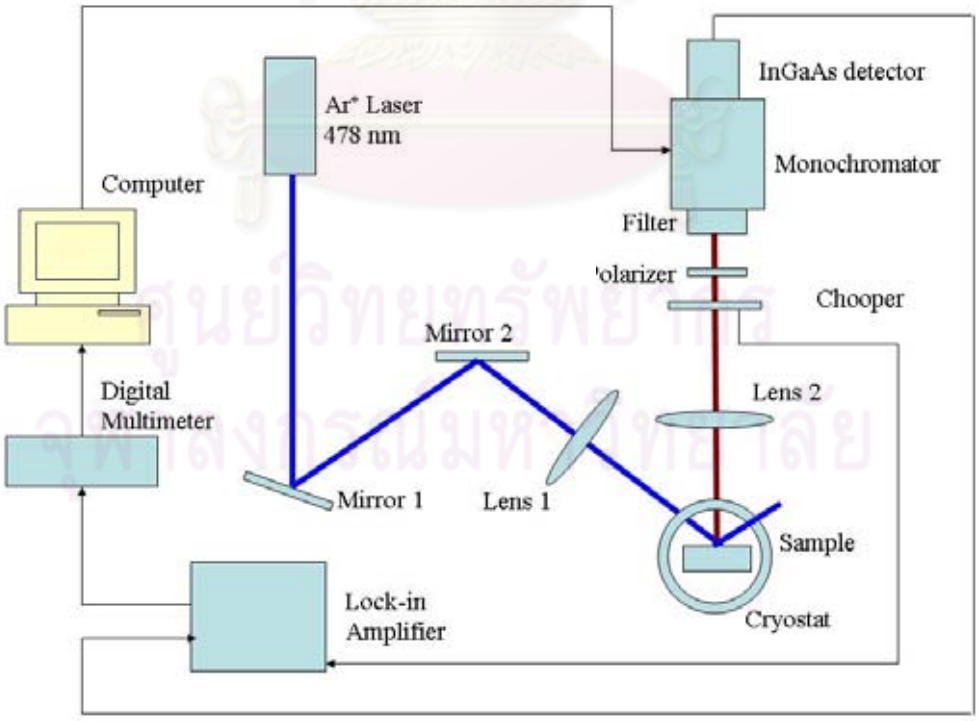

Figure 3.8 Schematic of the PL experimental setup

The PL result can provide the luminescence properties of a nanostructure system. In Figure 3.9, the ground state PL peak energy contains information about the size of the nanosturcture. The nanostructure with a larger size would have a lower quantized energy levels of both holes and electrons, which causes a lower PL peak energy position. Therefore, this PL peak position can be used to compare the size of nanostructures. In addition, the different size of nanostructures in an array can affect the shape of the PL spectrum as shown in Figure 3.10. A broadening of the spectrum, which is measured in terms of full width at half maximum (FWHM) or PL linewidth, is related to the nanostructure size distribution. Moreover, a polarization-resolved PL spectrum gives information on the nanostructure shape or nanostructure-system alignment in different crystal directions.

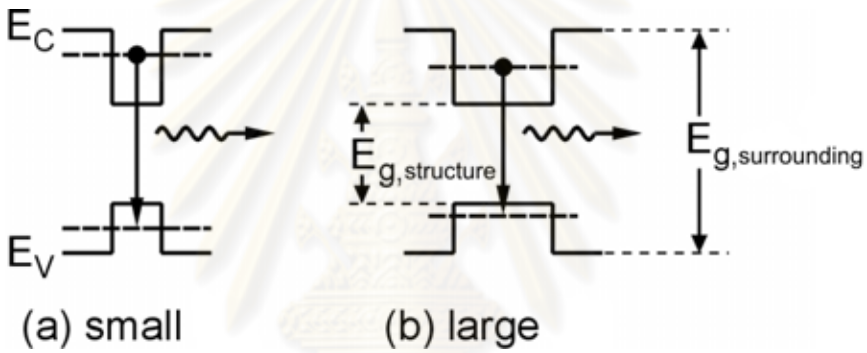

Figure 3.9 A simple interpretation of the PL data from a nanostructure; (a) higher PL peak energy position from a small-size nanostructure and (b) lower PL peak position from a large-size nanostructure.

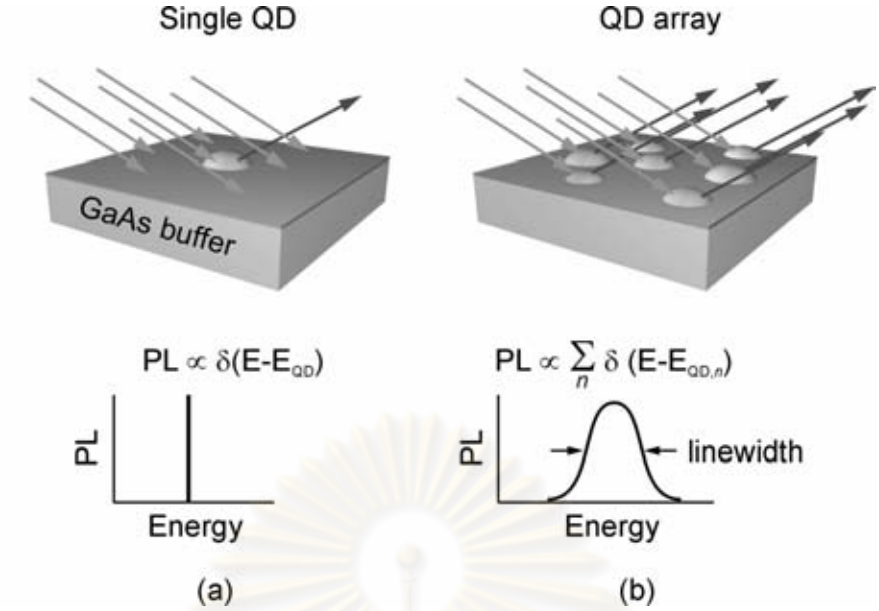

Figure 3.10 A comparative of the PL spectrum from a single QD and QD array; (a) narrow PL spectrum due to the delta-function like density of states of a QD. (b) The PL *peak* energy position and the PL *linewidth* interpreting the *average size* and the *size distribution* of the QD array, respectively.

3.5. Experimental Procedures

In this work, the samples of InGaAs QRs were fabricated on GaAs (100) substrates by droplet epitaxy using a RIBER 32P conventional solid-source MBE system. The growth conditions have been varied for droplet formation. A detailed sequence for sample preparation is as follows.

(1) Pre-heating: A piece of epi-ready semi-insulating (100) GaAs substrate was attached to a Mo (molybdenum) block (substrate holder) by indium glue. The block with the substrate was transferred to the introduction chamber and heated to 450^{o}C for 60 minutes in order to eliminate water vapor and oxide from the substrate.

(2) Deoxidation: After pre-heating, the sample (the substrate mounted on a Mo block) was transferred into the UHV growth chamber. The native oxide of the GaAs substrate surface was removed by slowly ramping up to 600^{o}C

under an As_4 flux of ~ 7×10^{-6} torr until a streaky RHEED showed a clear and abrupt pattern as shown in Figure 3.11.

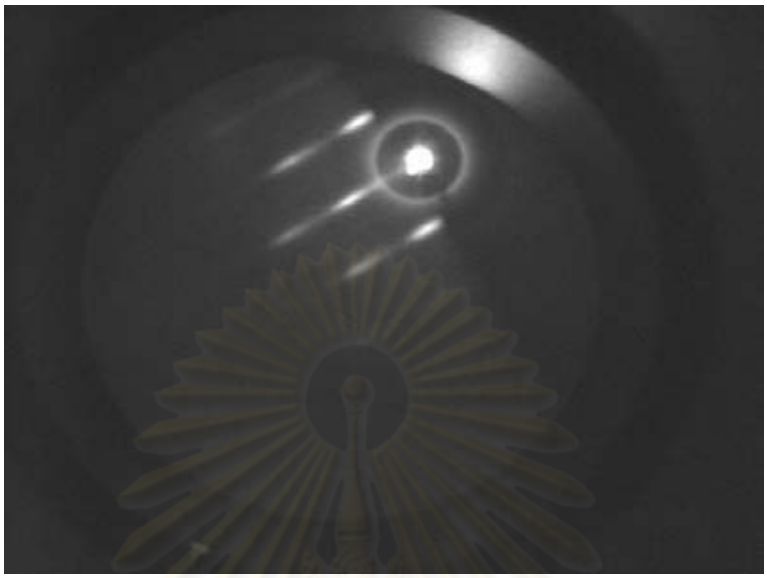

Figure 3.11 Streak RHEED pattern observed during the de-oxidation process.

(3) Growth of the GaAs buffer layer: a 300-nm thick undoped GaAs buffer layer was grown at 580°C to smooth the surface. The growth rate of GaAs was 1 monolayer/s (ML/s). A clear streaky (2×4) RHEED pattern was always observed after the growth of a buffer layer.

(4) Formation of InGa droplets: The growth conditions were varied in this step. First, the As_4 flux was turned off and the substrate temperature was lowered to 530°C to eliminate excess As atoms on the surface. Subsequently, the substrate temperature was decreased again to the desired deposition temperatures (T_s) in the absence of As_4. Then, the process was paused until the background pressure in the growth chamber was below 1 x 10^{-9} Torr to minimize the initial interaction between the InGa metal and background arsenic during droplet formation.

(4.1) to investigate the effect of T_s and deposited $In_{0.5}Ga_{0.5}$ amount on InGaAs QRs, 2-5 ML $In_{0.5}Ga_{0.5}$ (an equivalent amount of $In_{0.5}Ga_{0.5}As$ when

As_4 is supplied) was deposited at T_s = 120-300°C to form InGa droplets on GaAs layer. The deposition rate of $In_{0.5}Ga_{0.5}$ was 1 ML/s.

(4.2) to investigate the effect of Indium-mole-fraction (x), 3 ML In_xGa_{1-x} (x = 0.3 - 0.7) was deposited at T_s = 150°C to form InGa droplets. The deposition rate of In_xGa_{1-x} was 1 ML/s.

(5) Crystallization: After deposition, the substrate temperature was slowly ramped to 180°C within 11 min. Finally, the InGa droplets were exposed to 6-7×10^{-6} torr of As_4 flux at 180°C for 5 min to crystallize the metallic droplets into InGaAs QRs [6,23]. Note that crystallization was done at 180°C for all samples to prevent inter-diffusion of In atoms out of the droplets. A schematic illustration of the sample structure after crystallization is shown in Figure 3.12 (a). After the growth, the samples were taken out of the MBE system and examined for their surface morphology ex situ by atomic force microscopy (AFM: SEIKO SPA 4000) in tapping mode.

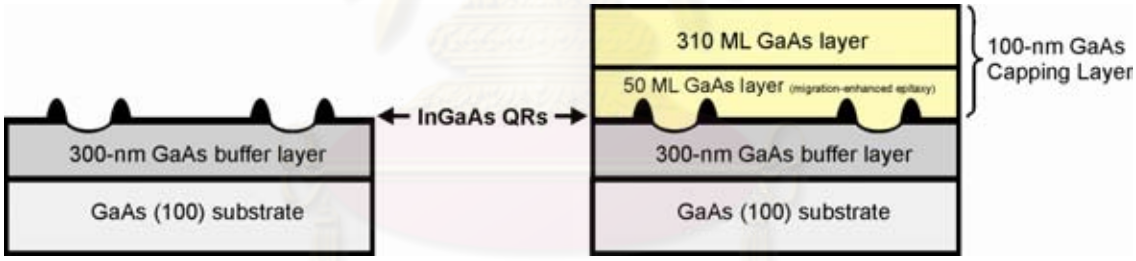

(a) (b)

Figure 3.12 Schematic illustrations of the sample structures grown in this work (a) after crystallization in As_4, and (b) after capping with a 100-nm GaAs capping layer. The details of growth sequences and growth conditions for the InGaAs nanostructures are given in the text.

(6) GaAs capping (for PL measurement): another series of samples were grown under the conditions of 2-5 ML $In_{0.5}Ga_{0.5}$ deposition at T_s = 210°C with an additional 100-nm GaAs capping layer grown by the two-step growth method. After the entire growth sequences (1-5), the substrate temperature was slowly increased to 300°C in As_4 flux. Then, to prevent the deformation

of uncapped droplet-originated InGaAs QRs, the capping layer growth started with a 50-ML-thick GaAs grown by MEE at 300°C, by alternately supplying 50 cycles of Ga for 2 seconds (0.5 ML/s), As for 2 seconds and interrupting for 2 seconds [55,56]. Subsequently, the substrate temperature was slowly increased again to 400°C in As_4 flux and a 310-ML-thick GaAs was grown at 400°C by the conventional growth method with a growth rate of 0.5 ML/s. The sample structure with a 100-nm GaAs capping layer is illustrated in Figure 3.12 (b).

CHAPTER IV

RESULTS AND DISCUSSIONS

In this chapter, the experimental results of InGaAs QRs grown by droplet epitaxy using MBE are shown. The droplet forming parameters, including the amount of $In_{0.5}Ga_{0.5}$ deposited, the substrate temperature during deposition (T_s), and the Indium-mole-fraction of In_xGa_{1-x} droplets are varied to study their effects on the InGaAs QR properties. By using atomic force microscopy (AFM), the effects of each droplet forming parameters on the size and density of the nanostructures are investigated. Finally, the QRs have been re-fabricated under selected droplet forming conditions with an additional GaAs capping layer for photoluminescence (PL) measurement. The optical properties of the InGaAs QRs have been investigated from PL spectra of the capped InGaAs-QR samples at 20-100 K.

4.1 Evolution of Surface Morphology

The evolution of surface morphology during growth was observed in situ by RHEED and recorded via a commercial CCD camera. Figure 4.1(a) shows the RHEED patterns of a GaAs buffer layer before $In_{0.5}Ga_{0.5}$ deposition. The (2x4) streaky patterns indicate a flat surface of the GaAs buffer layer. During 0-1 minute after $In_{0.5}Ga_{0.5}$ is deposited, the RHEED patterns dim and show no clear streak patterns, as shown in figure 4.1(b). This is attributed to the low density of InGa droplets formed on the surface. During 1-7 minutes after $In_{0.5}Ga_{0.5}$ deposition, the patterns are streaky patterns, as shown in figure 4.1(c). During 7-11 minutes after the deposition, the spotty RHEED patterns in figure 4.1(d) are clearly observed. From the time variation of the RHEED patterns, the mechanism of surface reconstruction can be explained. We can suppose that migration of In and Ga has occurred, causing the merging of neighboring droplets into larger droplets. We also suppose that there is the partial crystallization of droplets. At 11 minutes after the deposition, the crystallization under As_4 flux of 6-7 x 10^{-6} Torr BEP started. The RHEED patterns of QRs which consisted of streaks and spots [57] are shown in figure 4.1(e), indicating the formation of ring-like nanostructures.

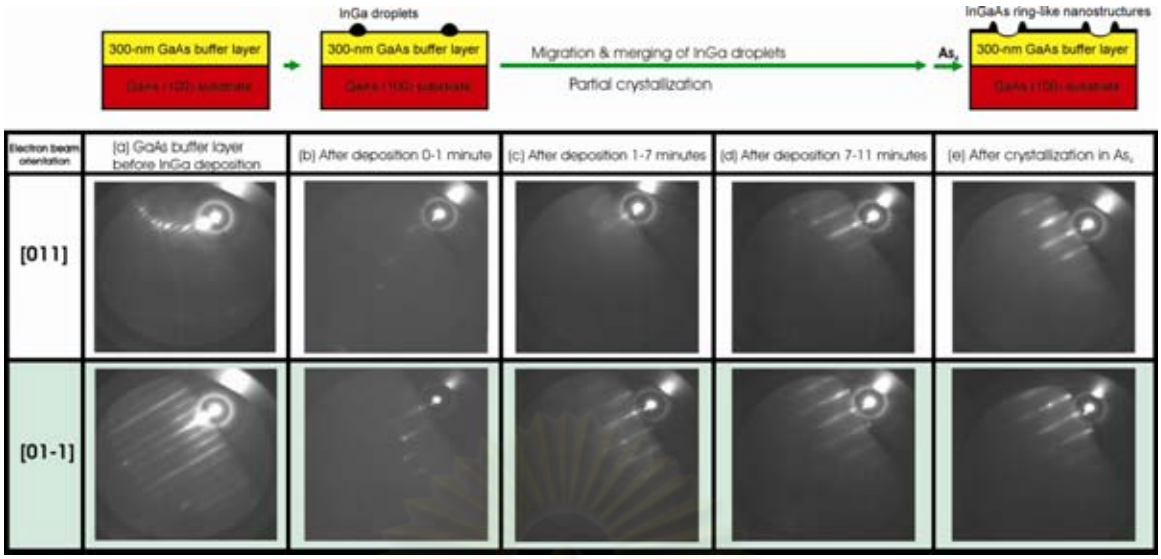

Figure 4.1 The formation process model of InGaAs QRs and RHEED patterns during the growth process. (a) RHEED patterns of 300-nm-thick GaAs buffer layers before $In_{0.5}Ga_{0.5}$ deposition, (b) RHEED patterns of the droplets during 0-1 minute after $In_{0.5}Ga_{0.5}$ deposition, (c) 1-7 minutes, (d) 7-11 minutes after depositing 3 ML $In_{0.5}Ga_{0.5}$, and (e) Streaky and spotty RHEED patterns after supplying As_4 flux of 6-7 x 10^{-6} Torr for 5 minutes, indicating the formation of InGaAs QRs. The incident orientation of electron beam is along the [011] and [01-1] direction.

The final RHEED patterns are different in the case of QD and QR. In the case of QD, the resulted RHEED pattern originates from the product of transmission and chevron pictures, schematically illustrated in Figure 4.2. On the other hand, in the case of QR, the resulted RHEED pattern originates from the transmission/reflection image and the reciprocal picture of the rotational structure, schematically illustrated in Figure 4.3 [57].

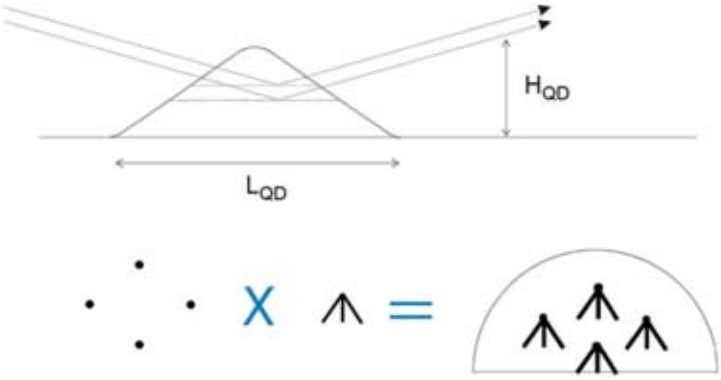

Figure 4.2 Scatterings of grazing electron beam on QD. Upper part: the geometrical arrangement of scattering on several crystal planes in QD. Transmission character dominates here. Lower part: the QD RHEED pattern originated from the product of the diffraction intensity from a crystal cluster and from a pyramid [57].

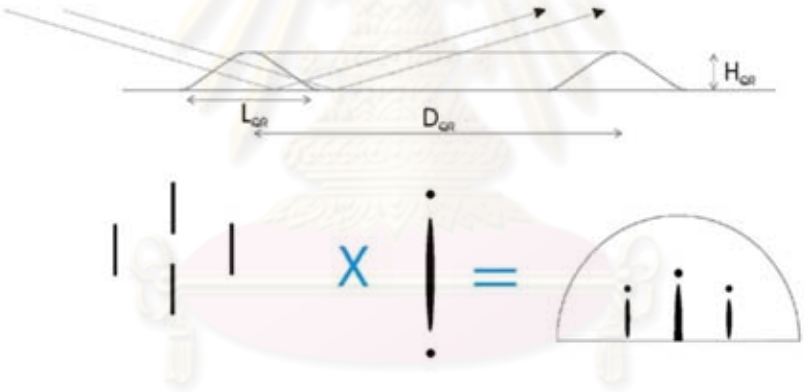

Figure 4.3 Scatterings of grazing electron beam on QR. Upper part: the geometrical arrangement of scattering on several crystal planes in QR or on two-dimensional basis plane. Either transmission or reflection character dominates depending in the finite size. Lower part: the product of transmission or reflection-like intensity and the scattering from rotational-shaped nanostructure resulting in near same RHEED pattern [57].

4.2 Surface morphology

The surface morphology of the crystallized samples was examined by tapping-mode AFM. Low-density InGaAs ring-like nanostructures, so called quantum rings (QRs), are observed. The QRs grown by droplet epitaxy technique have the density in the range of 10^7-10^8 cm^{-2}, which is low-density compared with SK grown QRs (of which density is typically in the range of 10^9-10^{11} cm^{-2}). From reports, the lowest densities of QRs formed by the conversion of SK grown QDs are in the range of ~ $10^9 cm^{-2}$, which is about the lower limit for SK QD formation [1]. Figure 4.4 shows 1000 x 1000 nm^2 2D top-view AFM images of InGaAs QRs grown under different droplet-forming conditions (varying T_s and $In_{0.5}Ga_{0.5}$ amount). The average QR outer diameter (nm), inner height (nm), outer height (nm), and density (× 10^8 QRs per cm^2) for each condition are also included. Note that depth of QRs is equal to different between inner height and outer height. The effects of each parameter are discussed in the next sections.

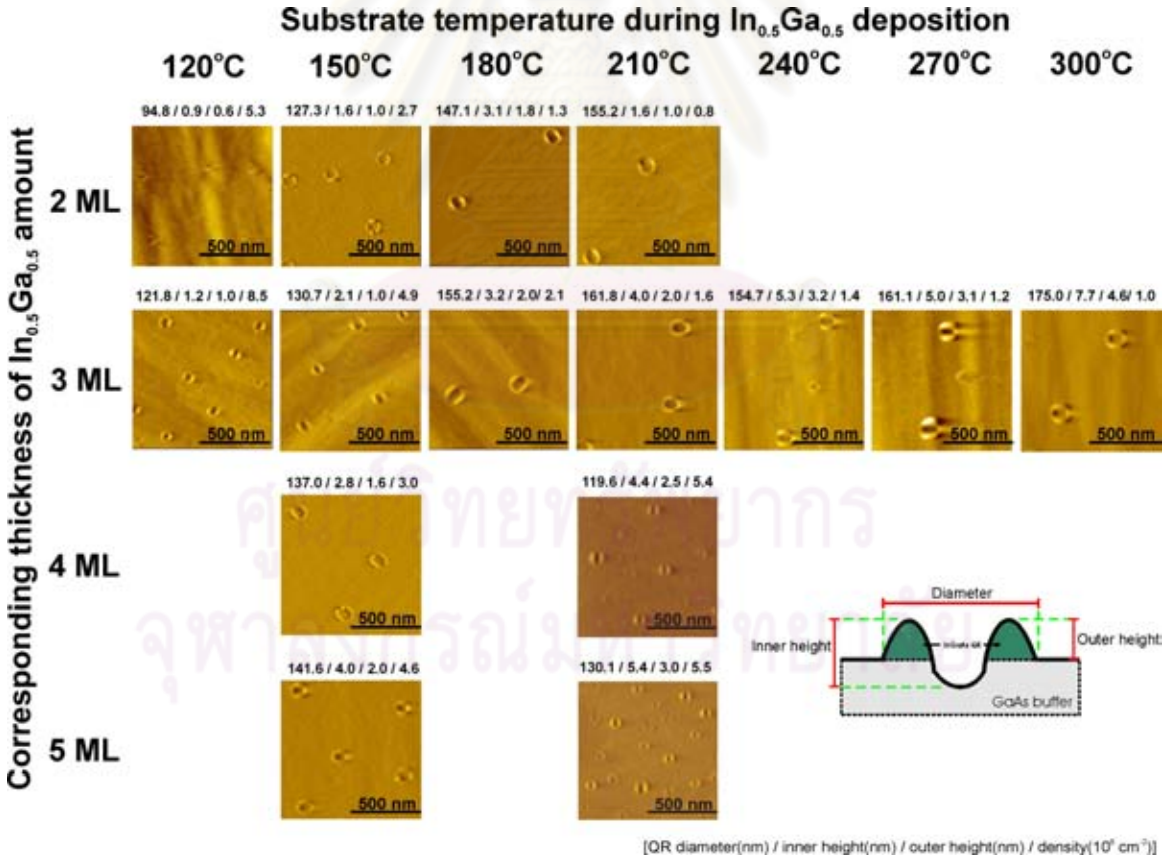

Figure 4.4 1000 x 1000 nm^2 surface morphology of InGaAs ring-like nanostructures grown on GaAs under different growth conditions, including T_s 120-300°C and $In_{0.5}Ga_{0.5}$ amount corresponding to epitaxial layer thickness 2-5 ML.

Figure 4.5 shows an example of 350 x 350 nm^2 surface morphology and the corresponding cross-sectional profiles along the [011] and [01-1] directions of a InGaAs QR grown under the condition of 3ML $In_{0.5}Ga_{0.5}$ deposition and 210°C substrate temperature. The nanostructures are not perfectly circular as seen by the elongation along the [01-1] direction (elongation ratio ~ 1.03-1.28). The elongation is due to anisotropic surface diffusion of group III atoms on GaAs (100) during the crystallization [58,59]. The surface diffusion is much higher along the [01-1] (i.e. surface diffusion coefficient at [01-1] is 4 times larger than that of [011]) due to the atomic corrugation of GaAs (100) induced by the reconstructed dimmer rows. Thus, a valid explanation for the elongation is there seems to be a lot of material *diffused away* along [01-1], also resulting in shallower QRs. Moreover, the center of the QRs is deeper than the substrate surface level due to *drilling effect* of metallic InGa droplets into GaAs matrix after the deposition [5,24]. Note that the QR diameters, the outer heights and the inner heights are obtained from the cross-sectional profiles of the QRs along the [011] direction.

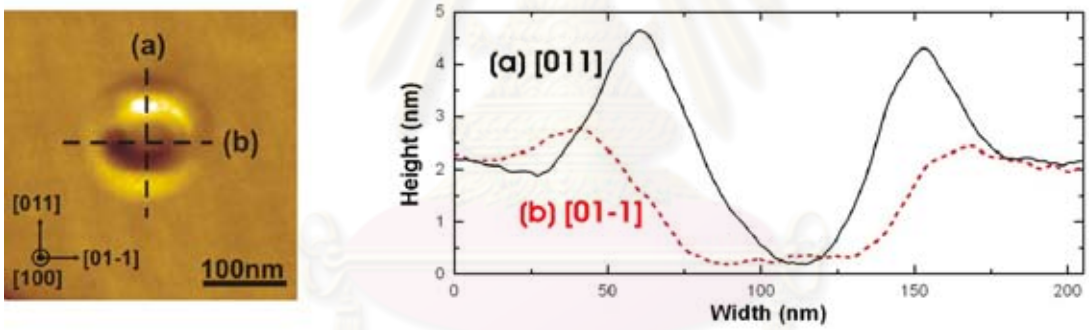

Figure 4.5 350 x 350 nm^2 AFM image and its cross-section along [011] and [01-1] of an InGaAs QR grown at 210°C with 3 ML $In_{0.5}Ga_{0.5}$ deposited.

The appearance of InGaAs ring-structures can be simply described. The formation mechanism of InGaAs ring-shaped nanostructures form metallic InGa droplets are roughly compared to the expansion mechanism of typical liquid droplets. The process is illustrated schematically in Figure 4.6. First, liquid-phase metallic InGa droplets are formed after the deposition of In and Ga atoms on the GaAs substrate (figure 4.6(a)). Like the liquid-phase droplets, the concentration gradient causes the diffusion of In and Ga atoms in the droplets. It results in 2-dimensional expansion of the droplets. At the moment, *drilling effect* of metallic droplets (along with interfacial intermixing process) and partial crystallization occur (figure 4.6(b)). The drilling effect is an etching process at

the interface between group III droplets and underneath III-V surface. At the interface between InGa droplets and the GaAs buffer layer, As atoms (associated with Ga) can be easily soaked into the droplets in order to equilibrate the energy between the GaAs matrix and the droplets. Since As atoms can not exist within the liquid droplets, the As atoms keeps travelling out of the droplets. Then, the As atoms either escape out of the droplets or interact with In and Ga atoms in the droplets, especially at the periphery of the droplets. Hence, InGaAs are formed at this zone, causing partially-crystallized InGa hemispherical-shaped structures [2]. At the same time, InGa droplets keep intermixing with underlying isolated Ga atoms (of which As was sucked out), forming metallic InGa right below the droplets. Second, during the crystallization under As_4 flux, the metallic In and Ga atoms from the droplets diffuse and interact with As atoms supplied on the nearby surface [4] and crystallized into InGaAs (figure 4.6(c)). Again, As atoms can not exist within the liquid droplets, so the efficient crystallization is expected at the bottom edge of the droplets [2,4,24]. As a result, InGaAs ring-shaped structures are formed surrounding the periphery of the droplets [2].

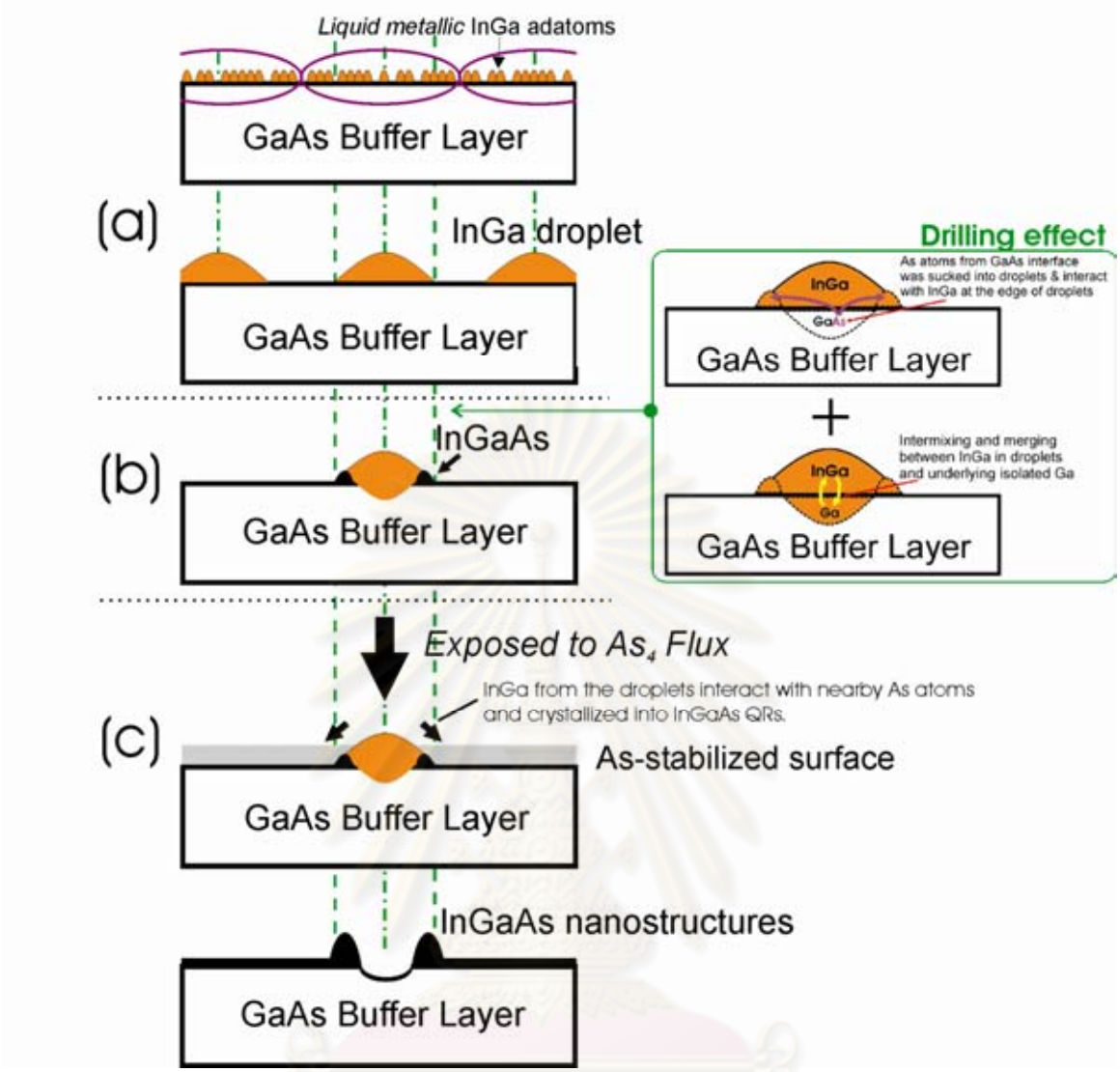

Figure 4.6 The formation mechanism model of InGaAs ring-shaped nanostructures (QRs) from metallic InGa droplets. (a) Formation of liquid-phase metallic InGa droplets from coalescence of deposited In and Ga atoms. (b) Drilling effect of droplets and partial crystallization. (c) The crystallization into InGaAs QRs under As_4 flux (QR diameter ~ droplet diameter).

4.3 Effects of substrate temperature during $In_{0.5}Ga_{0.5}$ deposition: T_s on InGaAs QRs

For the 1st series of samples, the nanostructures were formed under the condition of 2 ML $In_{0.5}Ga_{0.5}$ deposition at T_s = 120, 150, 180, and 210°C and under the condition of 3 ML $In_{0.5}Ga_{0.5}$ deposition on at T_s = 120, 150, 180, 210, 240, 270, and 300°C. Their morphological properties were examined. The dependence of the QR diameter and height on T_s is shown in Figure 4.7.

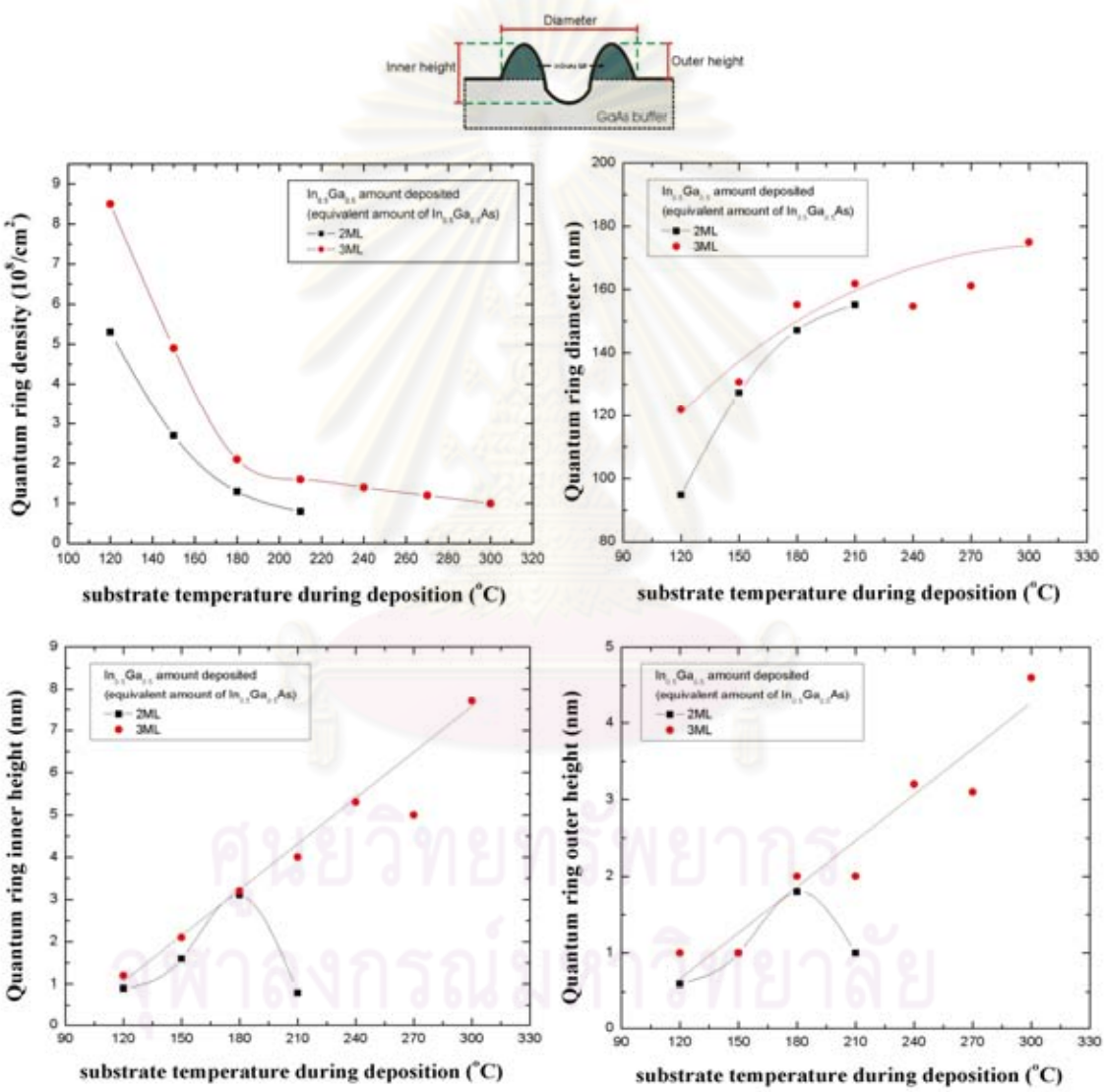

Figure 4.7 The dependence on substrate temperature (T_s) of InGaAs QR average size (diameter, outer height and inner height) and density.

While increasing T_s, the QR average size (typical outer diameter and the height of the QRs along [011]) increases but the density decreases. For example, when T_s = 120°C

under 3 ML $In_{0.5}Ga_{0.5}$ amount condition, the density was 8.5 x 10^8 cm^{-2} with QR diameter ~ 121 nm, the outer height ~ 1.0 nm, and the inner height ~1.2 nm. When T_s = 300°C, the density decreased to 0.9 x 10^8 cm^{-2} with diameter ~ 175 nm, the outer height ~ 4.6 nm, and the inner height ~ 7.8 nm.

The explanation is that the relatively large size of InGaAs QRs is due to the merging of neighbouring metallic InGa adatoms. The surface diffusion ability of metallic In and Ga atoms is proportional to the substrate temperature. Thus, at higher substrate temperature, the merging of InGa adatoms is increased, resulting in greater quantity of InGa in each droplet. After crystallization, fewer but larger InGaAs QRs are formed, as shown in Figure 4.8. Moreover, the increased surface diffusion ability also results in two-dimensional expansion of InGa droplets at high temperature. A schematic drawing of the 150-210°C 2-dimensional expansion is illustrated in Figure 4.9.

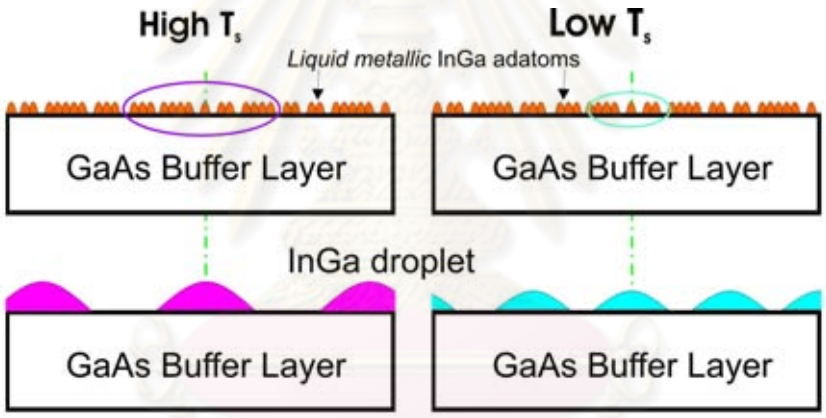

Figure 4.8 An illustration of different merging ranges of neighbouring metallic InGa adatoms at different substrate temperatures, showing larger size but lower density droplets at higher T_s.

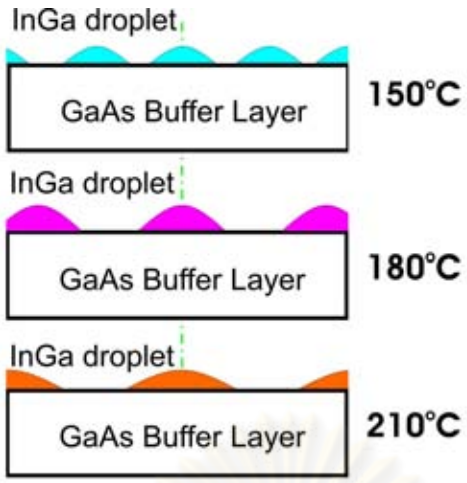

Figure 4.9 A schematic drawing of 2-dimentional expansion of QRs at different substrate temperature 150-210°C, showing wider expansion at higher T_s.

For 2 ML $In_{0.5}Ga_{0.5}$ deposition, we find that the heights of InGaAs QRs decreases at 180°C-210°C. Wider expansion of InGa droplets results in the decreasing of such droplet heights due to the limit of InGa amount deposited.

In addition, the dependence of InGaAs QR structural properties on T_s was investigated using the statistics of QR diameters, the outer heights, and the inner depths as presented in Figure 4.10 [60]. Morphological data of 50 QRs were collected for each T_s. Most InGaAs QRs have larger diameters and higher heights with increasing T_s. The diameter mostly varies between 155~200 nm and the outer height of the rings varies between 1.2~7.5 nm. However, at T_s = 300°C, the diameter distribution spread out more than the distribution at lower T_s. We suppose that *over-migration* of InGa in the droplets may occur at 300°C because of the high surface kinetics. As a result, some In and Ga atoms can migrate easier in-and-out of the droplets and merge with other droplet(s), causing the variation of droplet sizes before crystallization. Indefinitely, the InGa composition of nanostructures may not be entirely uniform due to the different surface kinetics [61]. Most inner depth of InGaAs QRs are virtually the same for various T_s. The inner depths varies between 0~6.5 nm.

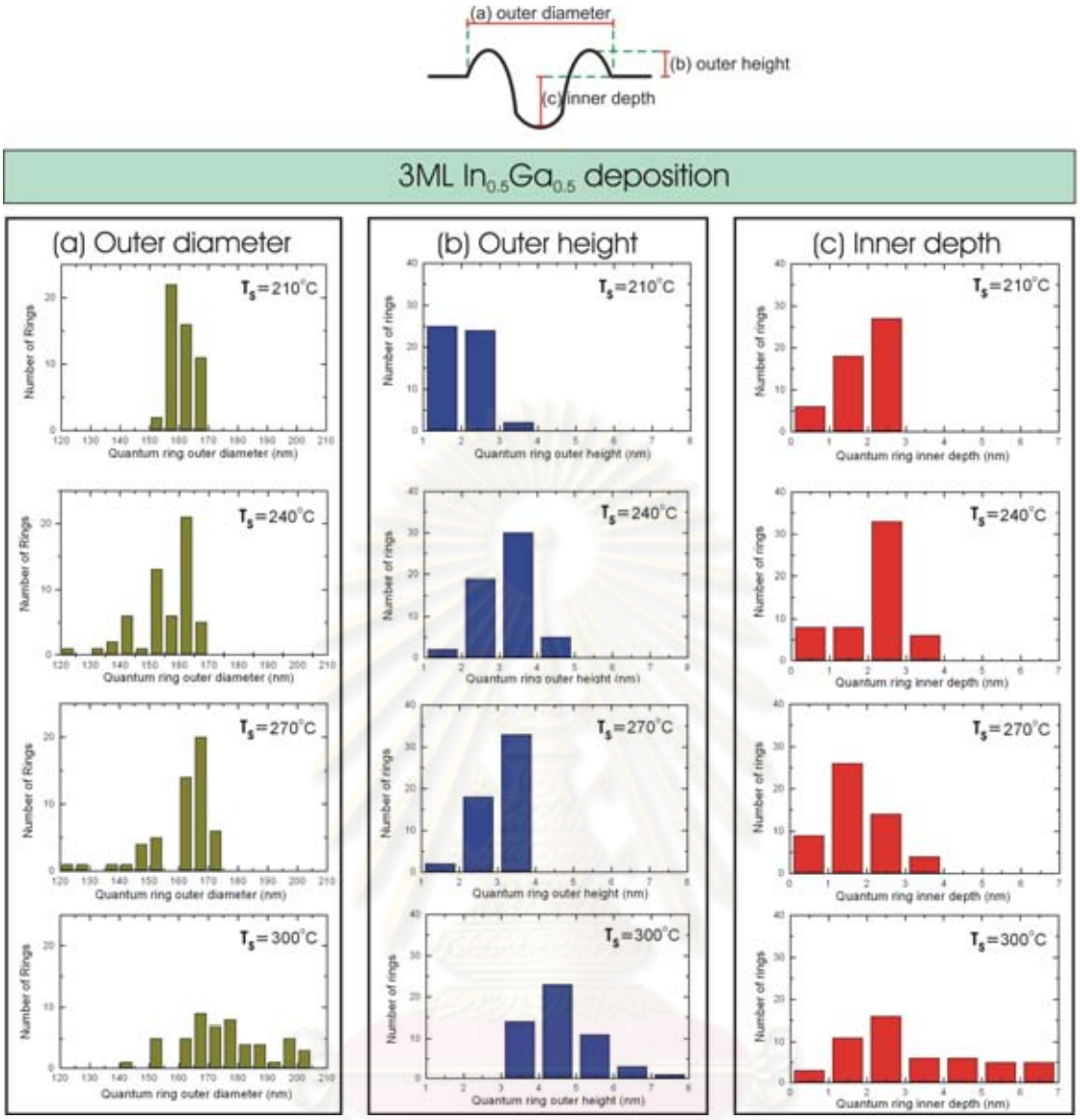

Figure 4.10 Dependence of InGaAs QR diameter, the outer height, and the inner depth on substrate temperature (T_s) during $In_{0.5}Ga_{0.5}$ deposition. The distributions of (a) outer diameter, (b) outer height, and (c) inner depth of InGaAs rings for each T_s: 210°C, 240°C, 270°C, and 300°C (data of 50 rings were collected for each condition) are presented. The $In_{0.5}Ga_{0.5}$ amount is 3 ML with a constant deposition rate of 1 ML/s

4.4 Effects of deposited $In_{0.5}Ga_{0.5}$ amount on InGaAs QRs

For the 2nd series of samples, the QRs were formed under the condition of 2, 3, 4, and 5 ML $In_{0.5}Ga_{0.5}$ deposition at 150°C and 210°C. The morphological properties of each sample were examined for their density and size, as shown in figure 4.11. In the case of 150°C substrate, the QR density oscillates every 2 ML $In_{0.5}Ga_{0.5}$ amount increasing. For 210°C, on the other hand, the ring density tends to saturate after 4 ML $In_{0.5}Ga_{0.5}$ deposition. The QR diameter and the height increase with increasing $In_{0.5}Ga_{0.5}$ deposited amount. However, at 210°C, the diameter decreases after 3-4 ML $In_{0.5}Ga_{0.5}$ deposition.

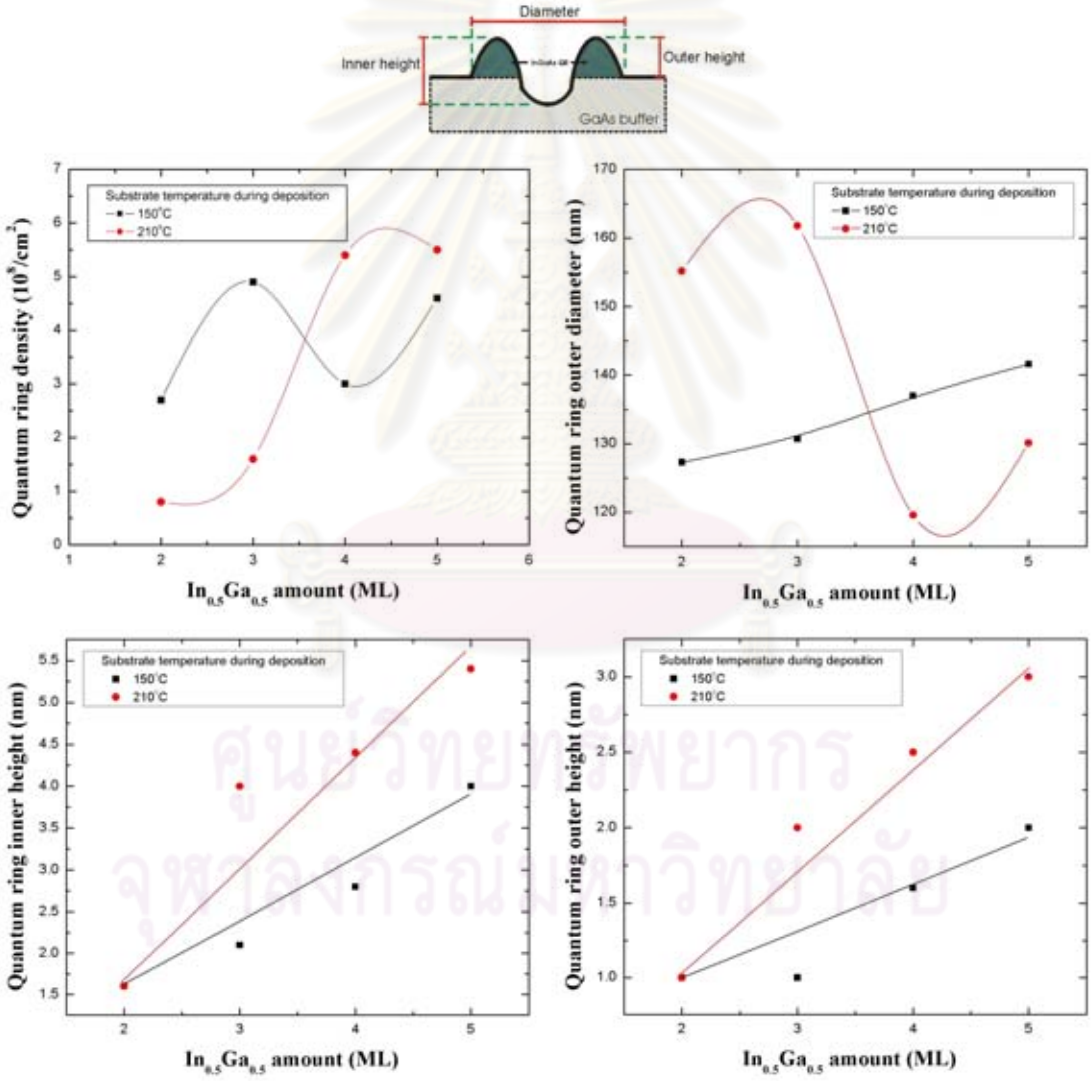

Figure 4.11 The dependence on deposited $In_{0.5}Ga_{0.5}$ amount of InGaAs QR size and density.

Considering the oscillations of QR density at T_s = 150°C, we suppose that there is the merging of metallic droplets into a full-layer. The illustration is shown in Figure 4.12. At the first 2-3 ML $In_{0.5}Ga_{0.5}$ deposited, the density of droplets increasing due to more InGa amount deposited. After the first 3 ML, there are enough small metallic-droplets covering full of the surface. The droplets then coalesce and form an InGa full-layer instead of individual droplets. The newly arrived InGa adatoms would form additional droplets above the layer. Hence, the density of the droplets has been renewed. For T_s = 210°C, on the other hand, the QR density increases during 2-4 ML and tends to saturate after 4-5 ML. Since at the higher T_s (210°C), the droplets are 22% larger but much lower density (70% lower than T_s = 150°C) due to higher surface energy and merging of droplets [see chapter 4.3, effects of T_s]. Therefore, more droplets are required to cover all of the surface. Considering the saturation of QR density, the full-layer takes place after the first 4 ML $In_{0.5}Ga_{0.5}$ deposited. Unlike 150°C, the droplets are so large that the upper part of the droplets still remains above the full-layer when InGa is increased to 5 ML. The newly arrived adatoms would add to the topmost part of the droplets, resulting in a saturation of droplet density. An illustration of each step is shown in Figure 4.13. Also, AFM images and corresponding cross-section of resulted QRs grown at 210°C with 2-5 ML $In_{0.5}Ga_{0.5}$ deposited are shown in Figure 4.14.

In the case of 210°C, the decrease of QR diameter during 3-4 ML is supposed to be caused from accumulated strain. Since the height of the droplets and the outer height of their corresponding InGaAs QRs after crystallization are higher than those of the 150°C case, compressive strain energy is accumulated inside the III-V structures. The relaxation then takes place at the QR-lateral center where the height reaches critical value. Considering hemispherical shape of crystallized QR lateral, when the center of QR lateral relaxes, their surrounding-edges are not relaxed as well (as thickness is not reach critical value as the center). This would limits strain to vertically relax to the top of QR. Thus, the vertical relaxation at center pulls the surrounding edge to the center (of QR lateral) along with increasing height. So, the base-size is forced to decrease with this process.

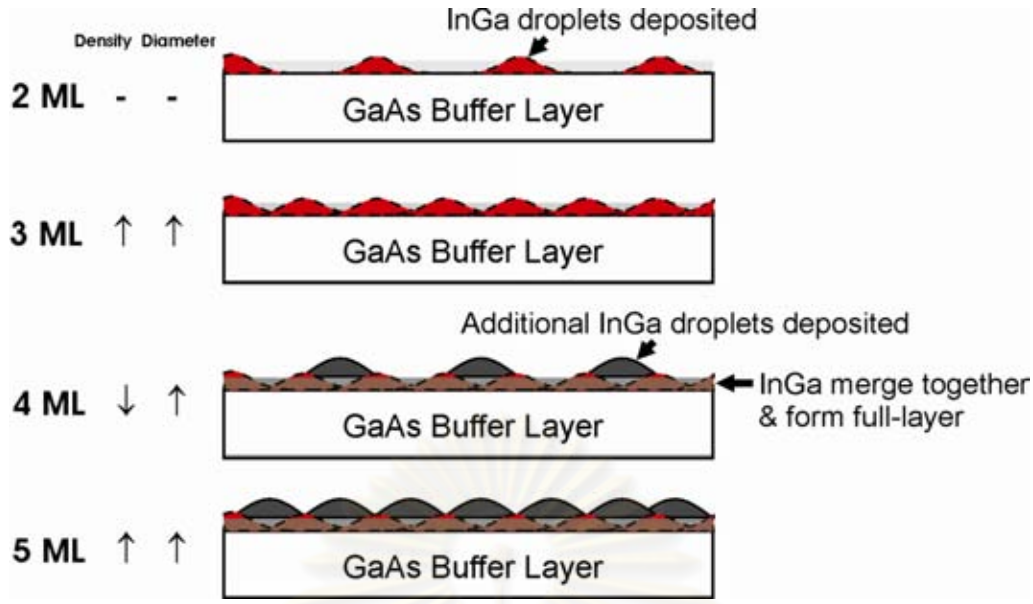

Figure 4.12 A schematic model of the reduction of QR density with increasing InGa amount, for $T_s = 150^oC$. The details are given in the text.

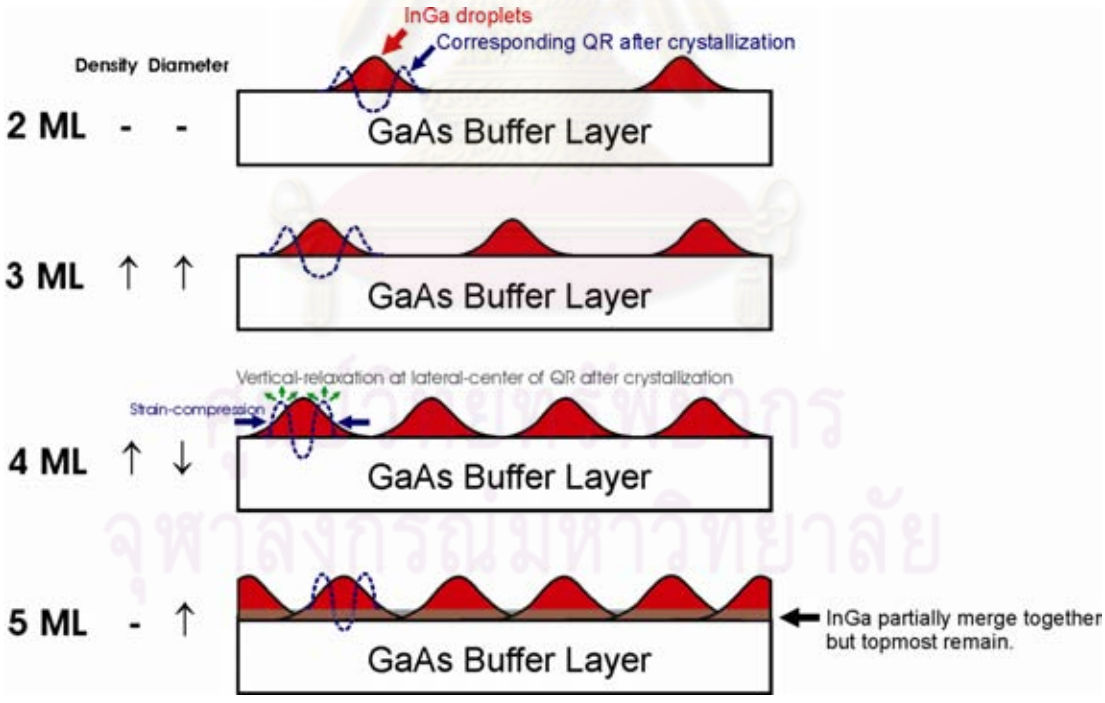

Figure 4.13 A schematic model of the saturation of QR density for $T_s = 210^oC$, including the drawing of corresponding crystallized QR to briefly describe diameter decreasing from the vertical-relaxation of the accumulating strain. The details of each step are given in the text.

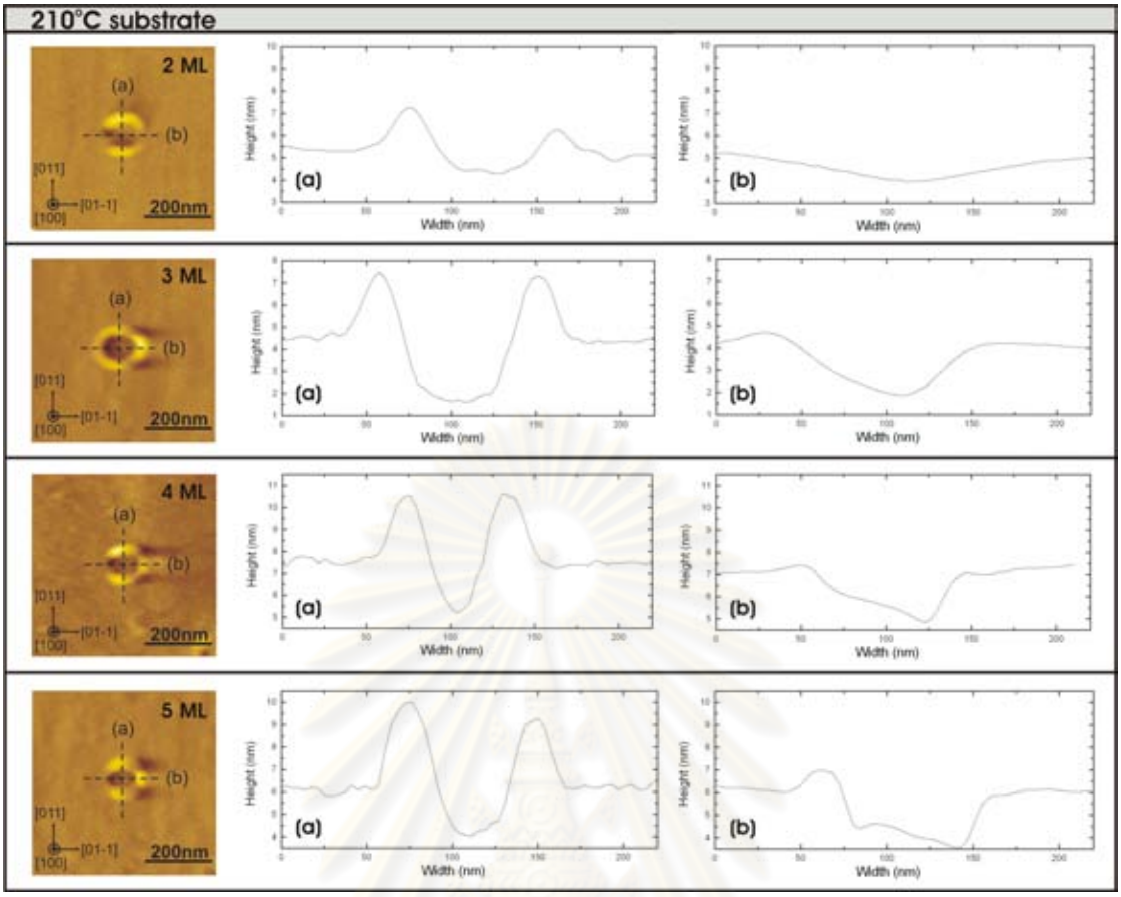

Figure 4.14 500 x 500 nm^2 AFM images and their corresponding cross-section along [011] and [01-1] of InGaAs QRs grown at 210°C with 2-5 ML $In_{0.5}Ga_{0.5}$ deposited.

4.5 Effects of In-mole-fraction of deposited In_xGa_{1-x} on InGaAs QRs

The size and density of the InGaAs QRs are strongly related to the In-mole-fraction (x). Figure 4.15 shows 500 × 500 nm^2 AFM images of the samples grown under the conditions of 3 ML In_xGa_{1-x} amount deposited ($0.3 \leq x \leq 0.7$) at 150°C and the corresponding QR-diameter distributions for each condition. The size of QRs can be clearly classified into 2 groups: subtle tiny-size QRs and obvious large-size QRs. With x = 0.3 and 0.4 (high-Ga-content), most QRs are tiny-size with average diameters of 47 and 58 nm, respectively, while only a few large-QRs exist (average diameter are 72 nm and 78 nm). The density of the tiny-size QRs is much higher than the large-size QR's, as shown in Figure 4.16. However, while increasing x to between 0.5 and 0.7, the density of tiny-size InGaAs QRs rapidly decreases and totally disappears. On the other hand, the

density of normal-size QRs slightly increases. With x = 0.5 - 0.7 (high-In-content), almost only low density large-size QRs are observed. Average QR diameters for x = 0.5, 0.6 and 0.7 are 131, 113 and 114 nm, respectively. The difference between the surface migration lengths of In and Ga atoms [53] is responsible for the difference of QR size and density. With increasing Indium content (x) beyond 0.5, the coalescence of liquid InGa droplets is strongly affected by the surface migration ability of high-In-content droplets. As a result, low density but bigger QRs are formed after crystallization. On the contrast, for x = 0.3 - 0.4, sticky *high-Ga-content* tiny droplets would form high density but tiny QRs after crystallization.

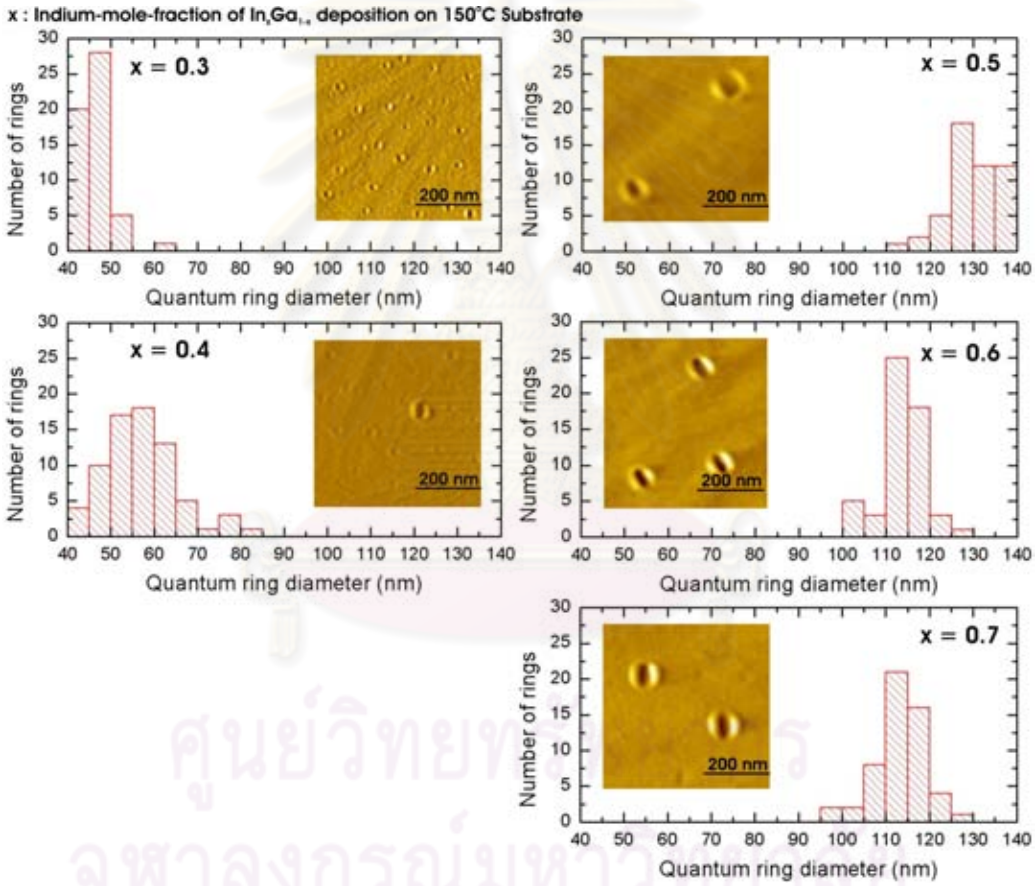

Figure 4.15 500×500 nm^2 AFM images of the samples grown under the conditions of 3 ML In_xGa_{1-x} deposited ($0.3 \leq x \leq 0.7$) at T_s = 150°C, including the corresponding QR diameter distributions for each condition.

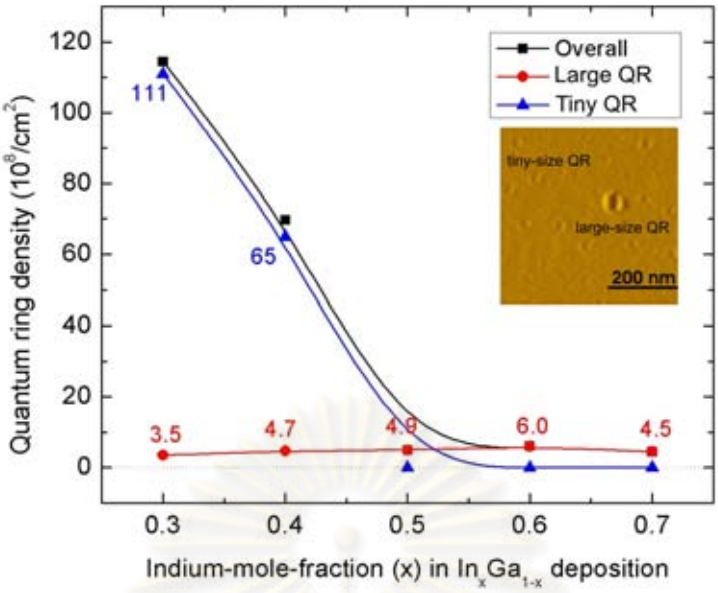

Figure 4.16 The dependence of the density of the tiny-size, large-size InGaAs QRs and overall (including both tiny-size and large-size QRs) on Indium-mole-fraction (x). Deposited In_xGa_{1-x} amount is 3 ML with T_s = 150°C.

4.6 Photoluminescence (PL) measurement of InGaAs QRs

Another set of samples were grown under the droplet forming condition of 2-5 ML $In_{0.5}Ga_{0.5}$ deposition at 210°C with an additional 100-nm GaAs capping layers. The capping layer included 50 ML of GaAs layer grown by migration-enhanced epitaxy (MEE) at 300°C and 310 ML of GaAs layer grown by conventional MBE method at 400°C. The optical properties of the InGaAs QRs were analyzed by PL spectra of the respective samples at 20-100 K.

For PL measurement, a 477 nm Ar^+ laser with power of 20-80 mW is used as the excitation source to characterize the optical properties of the capped InGaAs QRs at 20-100 K. PL emissions for 2 ML and 5 ML conditions are so low that we can not detect any signal from the samples. For 2 ML deposition, the density of QRs (0.8×10^8 cm^{-2}) is very low compared to the other conditions, resulting in very low signal from the sample. For 5 ML deposition, the PL emission efficiency may be degraded due to the accumulation of too much strain. Next, the PL spectra of the capped InGaAs QRs grown under the conditions of 3 ML and 4 ML $In_{0.5}Ga_{0.5}$ droplets deposited on 210°C substrate are examined under a reference measuring condition (exitation power = 40 mW, PL

measuring temperature = 20 K), as shown in Figure 4.17. The PL intensities are relatively low due to low density of the QRs (~ 1.6-5.4 × 10^8 cm^{-2}) and, probably, low-temperature crystallization which results in non-perfectly crystallization of QRs. Under the reference measuring condition, the PL spectra of the sample of 3 ML $In_{0.5}Ga_{0.5}$ droplet centers at 1017 nm (1.22 eV) with respective FWHM of 59 nm (77 meV). For the sample of 4 ML $In_{0.5}Ga_{0.5}$, the PL peak of 1007 nm (1.23 eV) with FWHM of 53 nm (65 meV) is detected. The peak of the 4 ML sample centers at a little shorter wavelength, corresponding with the relatively smaller size of 4 ML-condition QRs. Also, the PL intensity of the sample of 4 ML $In_{0.5}Ga_{0.5}$ is about 3 times higher than that of 3 ML sample, corresponding with the higher QR density (~ 5.4 × 10^8 cm^{-2} for 4 ML condition and 1.6 × 10^8 cm^{-2} for 3 ML condition). The slightly-broadening FWHM is due to 2 reasons; the size distribution of QRs [as shown in section 4.3] and the composition distribution. The composition of In and Ga in InGaAs may not be entirely uniform for all QRs due to randomly intermixing between InGa atoms in droplets and isolated Ga atoms at GaAs buffer interface during the interruption before crystallization [mentioned in section 4.2]. As a result, In and Ga composition are not exactly 0.5.

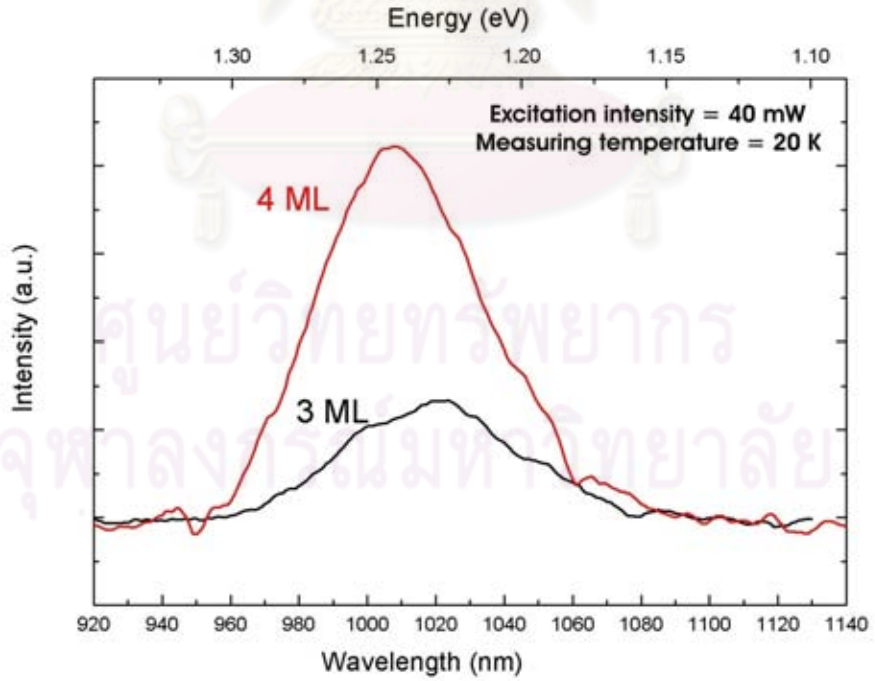

Figure 4.17 The PL spectra of the capped InGaAs QRs grown under the conditions of T_s = 210°C with 3 ML and 4 ML $In_{0.5}Ga_{0.5}$ droplets measured at reference PL measuring condition (laser power = 40 mW, measured at 20 K).

Excitation-power dependence photoluminescence

The PL spectra at 20 K of the samples as a function of excitation power are shown in Figure 4.18. As the excitation intensity increases, the PL intensities increase due to the increase of excess carriers by the excitation power. Also, the PL intensities increase without shifting and broadening while increasing the excitation power. Considering the discrete energy levels of the QR systems, only the ground-state peaks are observed (no state-filling effect). Approximated from the ground-state PL peak position of 1.22-1.23 eV, Indium-content of the QRs can be ~ 0.31-0.50 according to the experimental ground-state energies 1) of InAs/GaAs QDs with a potential well width ≤ 4 nm, which is 1.01-1.06 eV [62-65] and 2) of an $In_{0.5}Ga_{0.5}As$/GaAs QDs with well width of ≤ 4 nm, which is 1.17-1.23 eV [66,67].

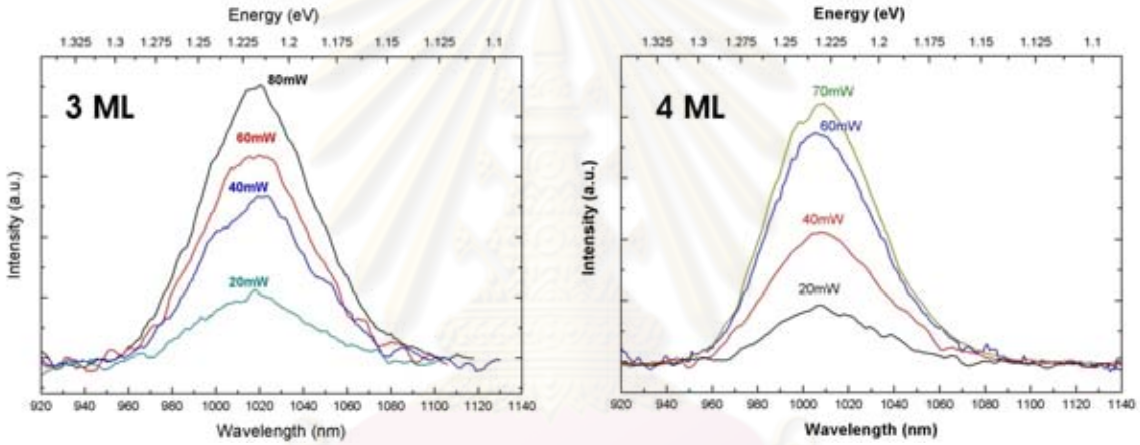

Figure 4.18 The PL spectra at 20 K with 20–80 mW excitation power of the capped InGaAs QRs grown under the conditions of T_s = 210°C with 3 ML and 4 ML $In_{0.5}Ga_{0.5}$ droplets.

Temperature dependence photoluminescence

The PL spectra as a function of measuring temperature are shown in Figure 4.19. The PL intensities decrease while increasing PL measuring temperature. The thermal excitation results in *less stability* of the carriers in QRs [68] and decreases probability of photon emission [69]. The equation used to fit with this result is the simple equation of the activation energy of quantum wells (Farfard et al., 1996)

$$I(T) = \frac{C}{1 + \alpha e^{-\frac{E_A}{kT}}} \qquad (4.1)$$

where C is constant, α is a fitting parameter, *k* is the Boltzmann's constant, and *T* is the measuring temperature. This equation indicates that PL intensity would decrease with increasing temperature. Even the thermal energy are small compared to the activation energy, there should be a certain part of carrier jump out of the nanostructures due to thermal excitation. By the way, the linewidths are invariant to the temperature change, confirming that thermal broadening is negligible.

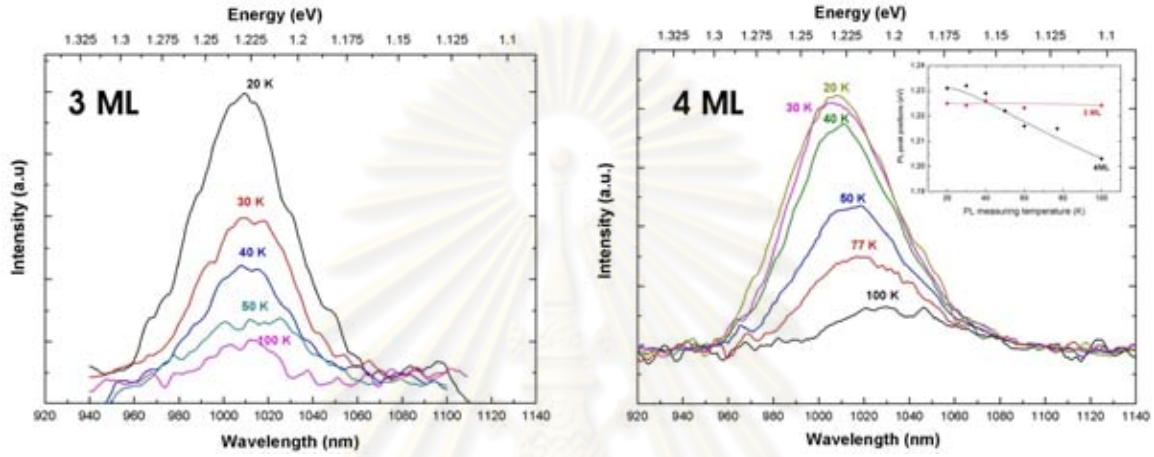

Figure 4.19 The PL spectra at 20-100 K of the capped InGaAs QRs grown under the conditions of T_s = 210°C with 3 ML and 4 ML $In_{0.5}Ga_{0.5}$ droplets (excitation power = 40 mW).

For the sample of 3 ML $In_{0.5}Ga_{0.5}$, the PL peak is *not shifted* while increasing the measured temperature from 20 K to 100 K. It indicates the *strain-free* QRs which create no strain effects on the energy band structures. So, the carriers hardly shift to any energy levels (strain-free may be considered as full relaxation of the thin-lateral 3 ML QRs, while the thicker-lateral QRs of 4 ML can accumulate more strain-field inside). Besides, the coupling properties supposedly support the invariant of the PL spectra to measuring temperature in addition to QR strain-free properties [70]. As shown in Figure 4.20, each of the anisotropic-lateral QRs may act like *coupled-QD*-pair. The QD diameter approximated to the QR-lateral width (~ 30-40 nm) and the distance between the adjacent QDs is ~ 40-50 nm at the center (not coupling) and < 10 nm at the ends (coupling). Overlap of the electronic wave functions in these coupled-like QDs causes a *small splitting* of energy state into two regenerated sub-levels [see section 2.1.2, also, Pauli's exclusion [71]]. Since, the splitting energy (ΔE) depends on inversion of distance between

adjacent QDs ($l_{C\text{-}QD}$), the energy of these two sub-levels is ~ $E_0 \pm \Delta E$, $\Delta E \propto 1/l_{C\text{-}QD}^2$ [39,72-75]. Thus, upon the increasing measuring temperature, the carriers can be thermally-excited to the higher-energy sub-levels, compensating the decreasing bandgap of Varshni's Law [69]. By the way, the small splitting can not be clearly detected in the excitation-power dependence PL due to relatively large FWHM.

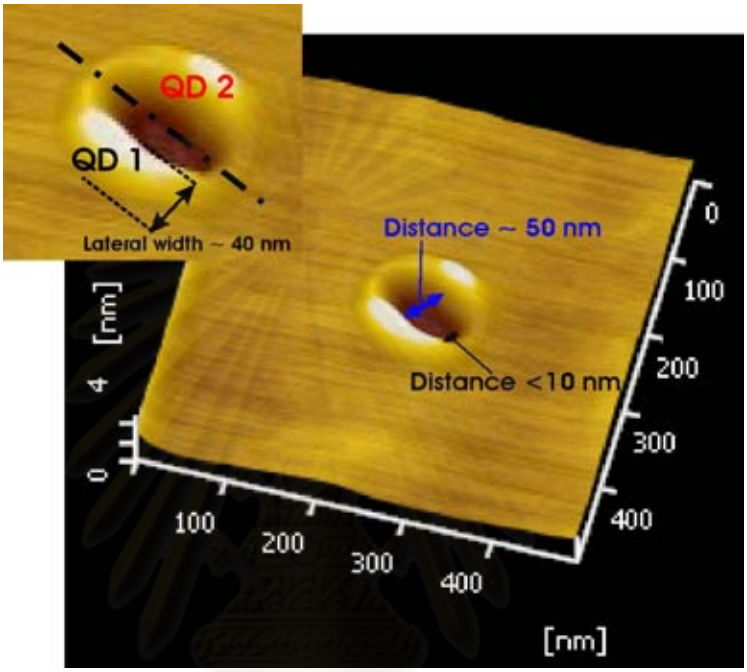

Figure 4.20 3-D AFM image of a QR with the illustration representing coupled-like QD corresponding with the anisotropic-laterals of the QR. The QD diameter is approximate to QR-lateral width (30-40 nm) and the distance between the adjacent QDs is ~ 40-50 nm at the center and < 10 nm at the ends.

However, for the 4 ML sample, the PL peak is 30 meV red-shifted while increasing the measured temperature from 20 K to 100 K. Although the main reason for this shift is the temperature dependence of the bandgap (Varshni's law [69]), the strain field is also supposed to partially accumulate inside the crystallized *thicker-lateral* QRs (higher outer height). The strain can complicate the energy band structures in which excited carriers have less stability [48,76]. This increases the possibility of the carriers to fall to the lower distorted energy levels and emit lower-energy photon with increasing thermal excitation.

Polarized photoluminescence

To characterize PL polarization, a linear polarization analyzer is used to obtain the polarization-resolved spectra. The polarization plane is parallel to (100) plane. The polarized PL spectra are shown in Figure 4.21. The crystal direction of [01-1] with a maximum PL intensity is used as the reference of 0^o. On 90^o turn of the analyzer from 0^o, the intensity deceases to the minimum (called 90^o, corresponding to [011] direction). The intensity of the 90^o-polarized spectrum (minimum) is 30% less than the 0^o-polarized spectrum (maximum). The polarized light is corresponding to the elongation along [01-1] of the QRs, confirming the non-perfect circularity or anisotropy of the QR structures [2,24,60].

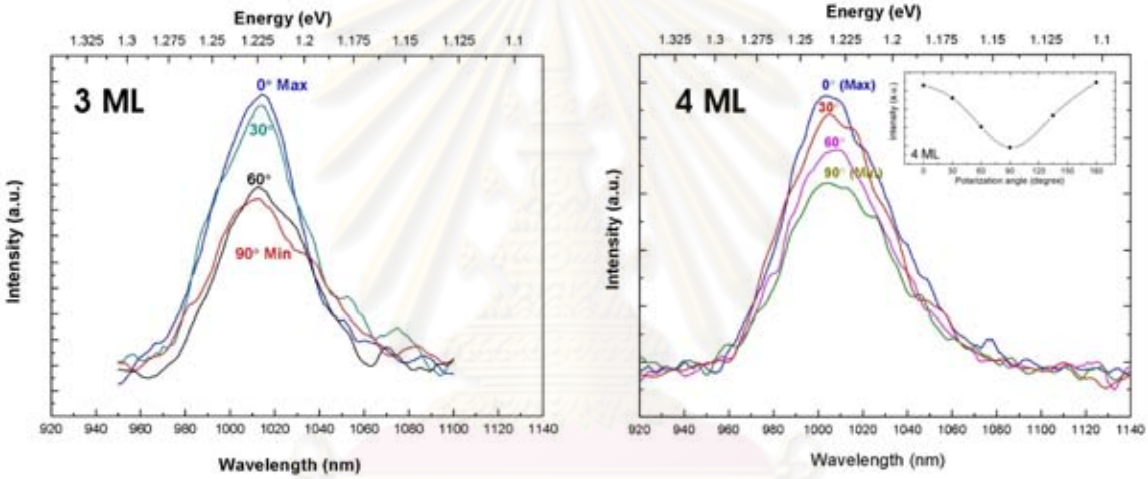

Figure 4.21 The PL spectra at various polarization angles: 0^o~[01-1], 90^o~[011] of the capped InGaAs QRs grown under the conditions of 210^oC substrate with 3 ML and 4 ML $In_{0.5}Ga_{0.5}$ droplets (measuring temperature = 20 K with laser power = 40 mW).

CHAPTER V

CONCLUSIONS

This work presents the fabrication of InGaAs ring-like nanostructures by droplet epitaxy using solid-source molecular beam epitaxy. The growth started with the formation of InGa droplets on GaAs surface and followed by the crystallization of the InGa droplets under As_4 pressure to form InGaAs quantum rings. During the growth, the evolution of surface structures was monitored by *in situ* RHEED observations. The formation mechanism of InGaAs quantum rings from metallic InGa droplets is investigated. After the crystallization, the surface morphology of the samples was characterized by ex situ atomic force microscopy. Low-density of $10^8/cm^2$ InGaAs quantum rings have been observed. The quantum rings are not perfectly circular due to anisotropy surface diffusion during the crystallization.

Furthermore, the growth conditions have been varied by changing the droplet forming parameters, i.e.; 1) substrate temperature during $In_{0.5}Ga_{0.5}$ deposition, 2) $In_{0.5}Ga_{0.5}$ amount deposited, and 3) In-mole-fraction of In_xGa_{1-x} droplets. The effects of each parameter on the morphological properties of the InGaAs quantum rings are investigated.

For the effects of substrate temperature during the deposition, it is found that increasing substrate temperature results in InGaAs quantum rings of a larger size but lower density. Greater migration length of In and Ga atoms leads to 2-dimensional expansion and coalescence of InGa into larger droplets. Thus, larger but fewer quantum rings are formed after the crystallization.

Regarding the effects of $In_{0.5}Ga_{0.5}$ amount, increasing the deposited $In_{0.5}Ga_{0.5}$ amount also results in changing of quantum ring size and density. At low substrate temperature, the quantum ring size increases with increasing $In_{0.5}Ga_{0.5}$ amount. However, the quantum ring density oscillates with increasing $In_{0.5}Ga_{0.5}$ amount. The oscillation is due to merging of numerous small droplets into a full layer instead of individual droplets. At higher substrate temperature, on the other hand, the increment of $In_{0.5}Ga_{0.5}$ amount results in quantum rings of a greater height, higher density but smaller diameter. The decrease of diameter is supposed to be caused by accumulating compressive strain inside the larger quantum rings and the partial relaxation.

Varying indium-mole-fraction of InGa droplets strongly leads to a variation of crystallized quantum rings. When indium content of InGa droplets is less than 0.5, high density tiny-size quantum rings are obtained after the crystallization. Whereas, when indium content is equal or more than 0.5, low density large-size quantum rings are formed after the crystallization.

The photoluminescence measurement was also performed to characterize the optical properties of the quantum rings. The InGaAs quantum rings were grown under selected conditions of 2-5 ML $In_{0.5}Ga_{0.5}$ droplets deposition at 210^{o}C substrate, with additional 100-nm GaAs capping layers. The capping layers were grown by migration-enhanced epitaxy at lower growth temperature and followed by the conventional method at higher temperature. The optical properties of the quantum rings were examined by photoluminescence spectra of the respective samples. The photoluminescence intensities are relatively low due to low density of the quantum rings. In particular, photoluminescence emissions for 2 ML and 5 ML conditions are too low due to very low density of QRs and accumulating strain, respectively. However, the photoluminescence emissions for 3 ML and 4 ML conditions can be examined. The photoluminescence peak of the 4 ML sample is centered at a little shorter wavelength than that of the 3 ML sample. This corresponds with the relatively smaller size of 4 ML-condition quantum rings. The photoluminescence intensity of the 4 ML condition is about 3 times higher than that of the 3 ML. This is due to higher density quantum rings in the 4 ML sample. Moreover, the full-width at half-maximum is slightly broad due to quantum ring-size distribution and composition distribution.

The photoluminescence measuring parameters including excitation intensity, measuring temperature, and polarization have been varied. As the excitation intensity is raised, the photoluminescence intensities increase without shifting. The ground-state energies of the InGaAs quantum ring systems are identified from the emission peaks. When the measuring temperature increases, the photoluminescence intensities decrease without thermal broadening. It is also observed that the photoluminescence peaks of the 3 ML sample are not shifted. This can attribute to the strain-free quantum rings which create no strain effect on the energy band structures. On the other hand, the peaks of the 4 ML sample are red-shifted. This shift can attribute to the existence of the strain field, which complicates the energy band structures and decreases the stability of the carriers. This increases the possibility to emit the longer-wavelength

photon with increasing the thermal excitation. Finally, the elongation of the quantum rings is confirmed by the polarization resolved spectra. It is found that the polarized spectra along the perpendicular crystal directions exhibit the maximum difference of intensity. This corresponds to the anisotropy of the quantum rings.

Recommendations for further works

Due to the density of quantum rings grown by droplet epitaxy is relatively low, it is difficult to clearly study the optical properties of the quantum rings grown under some conditions. The multi-stack growth can increase the number of quantum rings per unit volume. However, the stability of ring shape in each stack should be confirmed. Also, the rapid thermal annealing (RTA) can improve the crystal quality of such low-temperature-crystallized quantum rings to obtain higher photoluminescence intensity.

REFERENCE

[1] Lorke, A., Luyken, R.J., Garcia, J.M., and Petoff, P.M. Jpn. J. Appl. Phys. Part 1 40 (2001): 1857-1859.

[2] Mano, T., and Koguchi, N. J. Crystal Growth 278 (2005): 108-112.

[3] Lee, J.M., Kim, D.H., Hong, H., Woo J.C., and Park S.J. J. Crystal Growth 212 (2000): 67-73.

[4] Mano, T., Watanabe, K., Tsukamoto, S., Fujioka, H., Oshima, M., and Koguchi, N. J. Crystal Growth 209 (2000): 504-508.

[5] Wang, Zh.M., Liang, B.L., Sablon, K.A., and Salamo, G.J. Appl. Phys. Lett. 90 (2007): 113120.

[6] Wang, Zh.M., Holmes, K., Shultz, J.L., and Salamo, G.J. phys. stat. sol. 202 (2005): R85.

[7] Jevasuwan, W., Panyakeow, S., and Ratanathammaphan, S. In-droplet-induced formation of InP nanostructures by solid-source molecular beam epitaxy. Microelectronic Engineering 84 (2007): 1548-1551.

[8] Warburton, R.J., et al. Nature 405 (2000): 926.

[9] Ivanov, M.V., and Schmelcher, P. J. Phys.: Condens. Matter 18 (2006) : 2963.

[10] Lorke, A., Luyken, R.J., Govorov, A.O., and Kottaus, J.P. Phys. Rev. Lett. 84 (2000): 2223.

[11] Aharonov, Y., Bohm, D. Phys.Rev. 115 (1959): 485-491.

[12] Kleemans, N.A.J.M., Bominaar-Silkens, I.M.A., Fomin, V.M., Gladilin, V.N., Granados, D., Taboada, A.G., Garcia, J.M., Offermans, P., Zeitler, U., Christianen, P.C.M., Maan, J.C., Devreese, J.T., and Koenraad, P.M. Physical Review Letters 99 (14) (2007): 146808-1/4.

[13] Offermans, P., et al. Appl. Phys. Lett. 87 (2005): 131902.

[14] Granados, D., and Garcia, J. M. J. Cryst. Growth 251 (2003): 213.

[15] Granados, D., and Garcy´a, J. M. Appl. Phys. Lett. 82 (2003): 2401.

[16] Kiravittaya, S., Songmuang, R., Jin-Phillipp, N. Y., Panyakeow, S., and Schmidt, O. G. J. Cryst. Growth 251 (2003): 258.

[17] Schmidt, O. G., et al. IEEE J. Selected Topics in Quantum Electron 8 (2002): 1025.

[18] Songmuang, R., Kiravittaya, S., and Schmidt, O. G. J. Cryst. Growth 249 (2003): 416.

[19] Garc, J. M., et al. Appl. Phys. Lett. 71 (1997): 2014.

[20] Kobayashi, S., Jiang, C., Kawazu, T., and Sakaki, H. Jpn. J. Appl. Phys. 43 (2004): L662.

[21] Yu, L. W., Chen, K. J., Song, J., Xu, J., Li, W., Li, H. M., Wang, M., Li, X. F., and Huang, X. F. Advanced Materials 19 (2007): 1577.

[22] Koguchi, N., Takahashi, S., and Chikyow, T. J. Crystal Growth 111 (1991): 688.

[23] Lee, J.H., Wang, Zh.M., AbuWaar, Z.Y., Strom, N.W., and Salamo, G.J. Nanotechnology 17 (2006): 3973.

[24] Lee, J.H., Wang, Zh.M., Ware, M.E., Wijesundara, K.C., Garrido, M., Stinaff, E.A., and Salamo, G.J. Cryst. Growth Des. 8 (6) (2008): 1945-1951.

[25] Mano, T., et al. Nano Lett. 5 (2005): 425.

[26] Huang, S., Niu, Z., Fang, Z., Ni, H., Gong, Z., and Xia, J. Appl. Phys. Lett. 89 (2006): 031921.

[27] Watanabe, K., Koguchi, N., and Gotoh, Y. Jpn. J. Appl. Phys. 39 (1) (2000): L79.

[28] Alonso-Gonzalez, P., Alen, B., Fuster, D., Gonzalez, Y., and Gonzalez, L. Appl. Phys. Lett. 91 (2007): 163104.

[29] Kim, J.S., and Koguchi, N. Appl. Phys. Lett. 85 (2004): 5893.

[30] Yu, P.Y., and Cardona, M. Fundamentals of semiconductors: physics and materials properties. 2nd edition. Berlin: Springer-Verlag, 1999.

[31] Kittel, C. Introduction to solid state physics. 7th ed. New York: Wiley, 1996.

[32] Bimberg, D., Grundmann, M., and Ledentsov, N.N. Quantum dot heterostructures. Chichester: Wiley, 1999.

[33] Sugawara, M. Theoretical Bases of the Optical Properties of Semiconductor Quantum Nano-Structures. In M. Sugawara (ed.), Semiconductors and semimetals vol.60: Self-Assembled InGaAs/GaAs Quantum Dots, pp.1-116. San Diego: Academic Press, 1999.

[34] Bhattacharya, P. Semiconductor optoelectronic devices. New Jessy: Prentice-Hall Inc., 1994.

[35] Bastard, G., and Brum, J.A. Electronic states in semiconductor heterostructures. IEEE Journal of Quantum Electronics QE-22 (1986): 1625-1644.

[36] Arakawa, Y., and Sakaki, H. Multidimensional quantum well laser and temperature dependence of its threshold current. Appl. Phys. Lett. 40 (1982): 939.

[37] Asada, M., Miyamoto, Y., and Suematsu, Y. Gain and the threshold of three-dimensional quantum-box lasers. IEEE Journal of Quantum Electronics QE-22 (1986): 1915-1921.

[38] Zhukov, A.E., et al. 3.5 W continuous wave operation from quantum dot laser. Materials Science and Engineering B 74 (2000): 70-74.

[39] Harrison, P. Quantum Wells, Wires & Dots. 2nd edition. Chichester: Wiley, 2005.

[40] Bayer, M., Korkisinski, M., Hawrylak, P., Gutbrod, T., Michel, M., and Forchel, A. Phys. Rev Lett. 90 (2003): 186801.

[41] Ribeiro, E., Govorov, A.O., Carvalho, W.Jr., and Medeiros-Ribeiro, G. Phys. Rev. Lett. 92 (2004): 126402.

[42] Cheng, K.A., and Yang, C.H. Nanometer-size InAs/AlSb quantum wires: Fabrication and characterization of Aharonov–Bohm quantum rings. J. Appl. Phys. 88 (9) (2000): 5272-5276.

[43] Manninen, M., Koskinen, P., Koskinen, M., Viefers, S., and Reimann, S.M. Energy spectra and electron localization in quantum rings and dots [online]. 2004. Available from: https://www.jyu.fi/fysikka/en/research/material/clusters/download/matti-india.pdf [2010, October 20]

[44] Herman, M.A., and Sitter, H. Molucular beam epitaxy fundamentals and current status. Berlin: Spinger-Verlag, 1989.

[45] Leonard, D., Krishnamurthy, M., Reaves, C.M., Denbaars, S.P., and Petroff, P.M. Appl. Phys. Lett. 63 (1993): 3203.

[46] Suraprapapich S., Panyakeow, S., and Tu, C.W. Appl. Phys. Lett. 90 (2007): 183112.

[47] Seifert, W., et al. In-situ growth of quantum dot structures by the Stranski-Krastanow growth mode. Crystal Growth and Characterization 33 (1996): 423-471.

[48] O'Reilly, E.P. Valence band engineering in strained-layer structures. Semiconductors Science and Technology 4 (1989): 121-137.

[49] Kokuchi, N., and Ishige, K. Jpn. J. Appl. Phys. 32 (1993): 2052.

[50] Chikyow, T., and Koguchi, N. Jpn. J. Appl. Phys. 29 (1990): L2093.

[51] Koguchi, N., Ishige, K., and Takahashi, S. J. Vac. Sci. & Technol. B11 (1993): 787.

[52] Chikyow, T., and Koguchi, N. Appl. Phys. Lett. 61 (1992): 2431.

[53] Mano, T., Watanabe, K., Tsukamoto, S., Fujioka, H., Oshima, M., and Koguchi, N. Jpn. J. Appl. Phys. 38 (1999): L1009-L1011.

[54] Horikoshi, Y. Appl. Surface Science 65-66 (1993): 560-568.

[55] Horikoshi, Y., Kawashima, M., and Yamaguchi, H. Jpn. J. Appl. Phys. 27 (1988): 169.

[56] Horikoshi, Y., Kawashima, M., and Yamaguchi, H. Jpn. J. Appl. Phys. 25 (1986): L868.

[57] Nemcsics, A., Heyn, Ch., Stemmann, A., Schramm, A., Welsch, H., and Hansen, W. Materials Science and Engineering B 165 (2009): 118-121.

[58] Ito, T., and Shiraishi, K. Jpn. J. Appl. Phys. 37 (1998): 4234.

[59] Ohta, K., Kojima, T., and Nakagawa, T. J. Crystal Growth 95 (1989): 71-74.

[60] Pankaow, N., Panyakeow, S., and Ratanathammaphan, S. J. Crystal Growth 311 (2009): 1832-1835.

[61] Sablon, K.A., Wang, Z.M., and Salamo, G.J. Nanotechnology 19 (2008): 125609.

[62] Yamaguchi, K., Kaizu, T., Yujobo, K., and Saito, Y. J. Crystal Growth 237-239 (2009): 1301-1306.

[63] Celibert, V., Tranvouez, E., Guillot, G., Bru-Chevallier, C., Grenouillet, L., Duvaut, P., Ballet, P., and Million, A. J. Crystal Growth 275 (1-2) (2005): e2313-e2319.

[64] Lee, J.C., and Wu, Y.F. Intersublevel Relaxation Properties of Self-Assembled InAs/GaAs Quantum Dots Heterostructures. In Dragica Vasileska (ed.), Cutting Egde Nanotechnology, pp. 305-322: Intech, 2010.

[65] Heitz, R., Born, H., Guffarth, F., Stier, O., Schliwa, A., Hoffman, A., and Bimberg, D. Phys. Stat. Sol. (a) 190 (2) (2002): 499-504.

[66] Kalevich, V.K., and Tkachuch, M.N. Physics of the Solid State 41 (5) (1999): 789-792.

[67] Wahab, et al. Photoluminescence studies of $In_{0.5}Ga_{0.5}As$/GaAs quantum dots. In Proceeding of Annual Fundamental Science Seminar 2006 (AFSS 2006), 6th-7th June 2006 at Universiti Teknologi Malaysia, Skudai, Malaysia, 2006.

[68] Marcinkevicius, S., and Leon, R. Phys. Rev. B 59 (1999): 4630-4633.

[69] Bhattacharya, P. Semiconductor Optoelectronic Devices. 2nd edition. NJ: Prentice Hall International Inc., 1996.

[70] Mazur, Y.I., et al. Carrier Transfer in the Arrays of Coupled Quantum Dots. In Z. M. Wang (ed.), Self-Assembled Quantum Dots, pp.67-93. Springer, 2008.

[71] Gasiorowicz, S. Quantum Physics. 3rd edition. Hoboken: Wiley, 2003.

[72] Levi, A.F.J. Applied Quantum Mechanics. Cambridge: Cambridge University Press, 2003.

[73] Ben-Daniel, D.J., and Duke, C.B. Space charge effect on electron tunneling. Phys. Rev. 152 (1966): 683.

[74] Juang, C., Kuhn, K.J., and Darling, R.B. Electric field effects in AlGaAs-GaAs symmetric and asymmetric coupled quantum wells. IEEE Journal of Quantum Electronics 9 (1991): 27.

[75] Jing, C., Fernando, L., and Frensley, W.R. An efficient method for the numerical evaluation of resonant states. J. Appl. Phys. 76 (1994): 2881.

[76] Barker, J.A., Warburton, R.J., and O'Reilly, E.P. Phys. Rev. B 69 (2004): 035327.

Appendix

List of Publications

1. Pankaow, N., Panyakeow, S., and Ratanathummaphan, S. Nanometer-scale $In_{0.5}Ga_{0.5}As$ ring-like structure grown by droplet epitaxy. Advanced Materials Research 31 (2008): 123-125.

2. Pankaow, N., Panyakeow, S., and Ratanathummaphan, S. Fabrication of In0.5Ga0.5As ring-and-hole structure by droplet molecular beam epitaxy. Journal of Crystal Growth 311 (2009): 1832-1835.

3. Pankaow, N., Panyakeow, S., and Ratanathummaphan, S. InGaAs RING-SHAPED NANOSTRUCTURES GROWN BY DROPLET EPITAXY. Compound Semiconductor Photonics: Materials, Devices and Integration. (2010): 152-154.

4. Pankaow, N., Thainoi, S., Panyakeow, S., and Ratanathummaphan, S. Surface morphology and photoluminescence of InGaAs quantum rings grown by droplet epitaxy with varying In0.5Ga0.5 droplet amount. Journal of Crystal Growth (2011) (accepted, in press).

5. Pankaow, N., Panyakeow, S., and Ratanathummaphan, S. $In_xGa_{1-x}As$/GaAs Quantum Rings Grown by Droplet Epitaxy. AIP Proceedings of the International Conference on Physics of Semiconductor (ICPS2010) (2011) (accepted, in press).

List of Presentations

1. InGaAs/GaAs ring-like nanostructures grown by droplet using molecular beam epitaxy, Naraporn Pankaow, Somsak Panyakeow and Somchai Ratanathummaphan, 19th International Conference on Indium Phosphide and Related Materials (IPRM'07), Kunibiki Messe, Matsue, Japan, 14^{th}-18^{th} May, 2007.

2. Nanometer-scale $In_{0.5}Ga_{0.5}As$ ring-like structure grown by droplet epitaxy, Naraporn Pankaow, Somsak Panyakeow and Somchai Ratanathummaphan, 4^{th} International Conference on Materials for Advanced Technologies (ICMAT 2007), Singapore International Convention & Exhibition Centre, Singapore, 1^{st}-6^{th} July,2007.

3. Fabrication of In0.5Ga0.5As ring-and-hole structure by droplet molecular beam epitaxy, N. Pankaow, S. Panyakeow and S. Ratanathummaphan, 15^{th} International Conference on Molecular Beam Epitaxy (MBE 2008), University of British Columbia, Vancouver, Canada, 3^{rd}-8^{th} August, 2008.

4. InGaAs RING-SHAPED NANOSTRUCTURES GROWN BY DROPLET EPITAXY, Naraporn Pankaow, Somsak Panyakeow, Somchai Ratanathammaphan, International Conference on Materials for Advanced Technologies (ICMAT 2009), Suntec Centre, Singapore, 28^{th} May – 3^{rd} June, 2009.

5. Surface morphology and photoluminescence of InGaAs quantum rings grown by droplet epitaxy with varying In0.5Ga0.5 droplet amount, Naraporn Pankaow, Supachok Thainoi, Somsak Panyakeow, Somchai Ratanathammaphan, 16^{th} International Conference on Molecular Beam Epitaxy (MBE 2010), Berlin, Germany, 22^{nd}-27^{th} August, 2010.

6. $In_xGa_{1-x}As$/GaAs Quantum Rings Grown by Droplet Epitaxy, Naraporn Pankaow, Somsak Panyakeow, Somchai Ratanathammaphan, International Conference on Physics of Semiconductor (ICPS2010), Coex, Seoul, Korea, 25^{th}-30^{th} July, 2010.

VITAE

Naraporn Pankaow was born in Bangkok, Thailand on October 15th, 1983. She graduated from Chulalongkorn University demonstration in March 2001. In June 2001, she entered Chulalongkorn University and received the Bachelor of Engineering in field of Electrical Engineering with GPAX 3.35 in April 2005.

She continued her study in October 2005, as a master student. She received the Master degree of Engineering in Electrical Engineering Program in May 2007 from the Graduate School of Chulalongkorn University and furthered her study in October 2007, as a Ph.D. student. She was financially supported by Chulalongkorn University Graduate Scholarship to Commemorate the 72nd Anniversary of His Majesty King Bhumibol Adulyadej from October 2007 to November 2007. Since December 2007, she has received Royal Golden Jubilee Ph.D. Scholarship from Thailand Research Fund (Grant no. PHD/0011/2550).